Full Electromagnetic Integration of Impedance-Balanced EMI Filters for Single-Phase Power Converters

Shiqi Jiang, *Student Member, IEEE*, Panbao Wang, *Senior Member, IEEE*, Wei Wang, *Member, IEEE*, Yitao Liu, *Senior Member, IEEE*, and Dianguo Xu, *Fellow, IEEE*

***Abstract*—Utilizing passive electromagnetic interference (EMI) filters is the most widely used approach to restrain the conducted emissions from power converters. However, the introduction of these filters will significantly raise the weight and size of the systems. Using the emerging flexible multi-layer foil (FMLF) technique, this article investigates a complete electromagnetically integrated design concept of single-phase EMI filters based on EE-type cores, which can be applicable to engineering application scenarios with different EMI noise attenuation requirements. Two types of integrated structures are constructed with different well-designed FMLF-windings and terminal configurations. One is a common-mode (CM) choke with controllable leakage inductances, which is able to realize the integration design of CM inductor, CM capacitors and differential-mode (DM) inductors. The other is an EMI choke with integrating the CM and DM inductances and capacitances, which achieves electromagnetic integration of all the CM and DM filtering components. Compared to the existing UU-type core based integration methods, the proposed methods can ameliorate the noise suppression performance while reducing filter's weight and volume. Theoretical analyses for modeling and design of the EMI chokes is presented. Then prototypes of different FMLFs-based EMI filters have been built for a 500 W 100 kHz SiC-MOSFET inverter, experiments demonstrate the feasibility and validity of the proposed structures.**

***Index Terms*—Choke, common-mode (CM), conducted emission, differential-mode (DM), electromagnetic integration, electromagnetic interference (EMI) filter, flexible multilayer foils (FMLFs).**

I. Introduction

With the developments toward high-frequency and high-power-density of power converter systems (PCSs), reduction of conducted electromagnetic interference (EMI) has become a greater challenge in the design procedure, especially with the application of wide bandgap (WBG) semiconductors, such as silicon carbide (SiC) and gallium nitride (GaN) devices [1], [2], [3]. The fast switching motions associated with WBG devices lead to higher *dv/dt* and *di/dt*, which cause more serious EMI issues in PCSs. Some relevant electromagnetic compatibility (EMC) standards like IEC and EN have set the corresponding limits for conducted EMI levels with the frequency ranging from 150 kHz to 30 MHz in different application fields [4], [5]. It is necessary to restrict the noise amplitude in a PCS by some means to meet the requirements. As the mainstream means of diminishing the EMI emissions from PCSs, EMI filters are often indispensable.

Following the widespread utilization of passive EMI filters (PEFs), the optimization methods of PEFs for lightweight and miniaturization design have always been highly concerned by related scholars. As the most representative approach, passive integration techniques have been developed in great depth. The conventional magnetic integration techniques (CMITs) used in EMI filters are mainly aimed at the integration of inductors with various functions. In [6], a differential-mode (DM) choke with relatively low permeability is placed within the open window of the common-mode (CM) choke, both chokes share the same windings for integrated design of an EMI choke. In order to enhance the leakage inductances, the magnetic gel is used to be adhered around the CM choke in [7]. In this way, greater DM inductances can be obtained without extra DM chokes. In [8], based on the concept similar to that in [7], a built-up model is proposed with the CM choke embedded into an EQ-type core. Recently, some ameliorative magnetic integrated structures of EMI filters have been investigated. In [9] and [10], through utilizing an EE-core or the combination of a toroid and a solenoid, the CM and DM decoupling integrated EMI filters are modeled, analyzed and implemented, which give a full play of the CMITs.

The main drawback of CMITs is the limitation on promoting the integration-level for passive components. In this situation, the electromagnetic integration techniques (EMITs) that can be used to realize the integration design for both inductances and capacitances have been proposed for achieving a breakthrough. So far, there are two frequently-used types of EMITs: planar-winding and FMLFs-winding based techniques. In [11], the modeling and analyses of a planar-winding based *LC* cell are presented through the generalized transmission structure theory

Manuscript received 25 August 2022; revised 23 December 2022; accepted 14 February 2023. Date of publication 17 February 2023; date of current version 20 April 2023. This work was supported in part by Natural Science Foundation of Heilongjiang Province, China under Grant LH2022E067 and in part by the Natural Science Foundation of China under Grant 51977045. Recommended for publication by Associate Editor F. Dijkhuizen. *(Corresponding author: Panbao Wang.)*

Shiqi Jiang, Panbao Wang, Wei Wang, and Dianguo Xu are with the School of Electrical Engineering and Automation, Harbin Institute of Technology, Harbin 150001, China (e-mail: jiangshiqi@hit.edu.cn; wangpanbao@hit.edu.cn; wangwei602@hit.edu.cn; xudiang@hit.edu.cn).

Yitao Liu is with the College of Mechatronics and Control Engineering, Shenzhen University, Shenzhen 518060, China (e-mail: liuyt@szu.edu.cn).

Color versions of one or more figures in this article are available at https://doi.org/10.1109/TPEL.2023.3246177.

Digital Object Identifier 10.1109/TPEL.2023.3246177

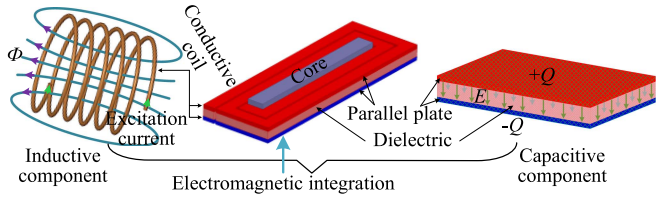

Fig. 1. Planar-winding based electromagnetic integration.

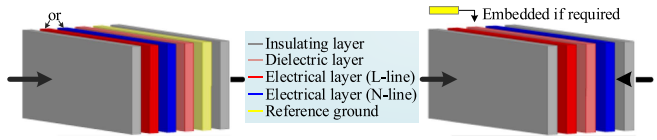

Fig. 2. Commonly used single-strip FMLFs.

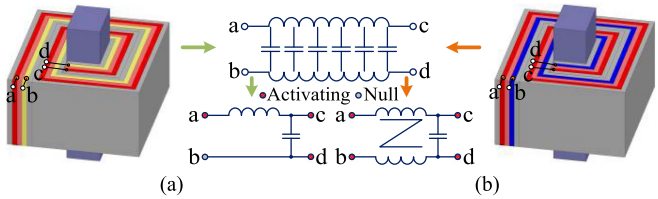

Fig. 3. Lumped equivalent filtering circuits of regular single-strip FMLFs under (a) CN-1, and (b) CN-2 activating modes.

discussed in [12]. It provides a basic concept for the integration of a coil inductance and a parallel plate capacitance, which can be described in Fig. 1. With the expansion of this technique, the concept of electromagnetic integration has been quickly introduced into design of EMI filters [13], and has been developed with different planar core and winding structures [14], [15], [16]. Different from planar EMITs, some flexible materials (mainly containing copper foils and dielectric film), instead of rigid materials, are used with FMLF techniques for winding design. The basic concept of both the techniques are similar, however, compared to planar EMITs, FMLF techniques can provide a more flexible and compact model to meet the design requirements. Moreover, the total length and footprint of the windings will be significantly reduced with FMLF techniques, which can improve the performance in many ways though the height of the integrated unit will be raised [17], [18], [19], [20]. According to the conclusions in [21] and [22], FMLF technique is a better candidate for the passive integration with high frequency, high stability, and low power loss due to the merits of its forming principles, layer configurations, and dielectric films with stable properties, it is suitable for EMI filter design in theory. For improving the system's power density from the perspective of EMI filters, an electromagnetically integrated CM choke and a fully integrated EMI choke are investigated in literature [17] and [23], respectively, with the FMLF technique. In the existing integrated CM choke, both the CM inductor and CM capacitors are integrated into the same core unit, the leakages of the CM inductance are used as the DM inductors. Although this model can attain satisfied CM noise suppression performance, its DM noise attenuation capacity is quite limited and uncontrollable. Therefore, extra discrete DM capacitors are generally required to be combined with this approach. In the existing fully integrated EMI choke, all the CM and DM filtering inductors and capacitors are integrated into the same unit, this model has great design potential for both the CM and DM noise suppression capacities, but the asymmetrical DM inductances will result in unbalanced impedances in *L*- and *N*-lines, this unbalance will tend to cause common mode-to-differential mode noise conversion, which is against to the EMI noise mitigation. Additionally, both the two kinds of filters mentioned above are designed with UU-cores, which generally require bulky magnetic core for antisaturation design, particularly for the design with DM inductors. From the perspective of engineering applications, ordinarily, in a typical EMI filter, CM filtering components are essential since the CM conducted noise is the main issue, while the DM components are generally flexibly configured considering the specific cases. In a grid-connected PWM converter system, the DM noise is often significantly mitigated by the prepositive harmonic filter, thus, just extra DM inductors or capacitors are sometimes sufficient for the DM noise abatement. In a PWM inverter-fed motor drive system, both the CM and DM noise issues are generally serious, hence, all the DM filtering components are usually required.

In order to compensate for the shortcomings of the existing electromagnetically integrated EMI filters while considering the applicability in common engineering practices mentioned above, this article investigates an ameliorative and complete EMI filter design method with the FMLF technique for different application scenarios. Taking integration design of CM filtering elements as the precondition, two types of electromagnetically integrated impedance-balanced EMI filters are constructed with EE-cores. One is a CM choke with controllable leakages (DM inductors), the other is an EMI choke with all the CM and DM filtering components integrated into the same unit. Considering the DM insertion loss (IL) design space and design difficulties of the proposed chokes, the two chokes are recommended as the better candidates for applications scenarios with relatively low and high DM EMI noise attenuation requirements, respectively. Compared to the aforementioned state-of-the-art EMI chokes, the proposed EMI chokes not only can improve the deficiencies in EMI suppression performance, but also can reduce the weight and size. Finally, prototypes of the integrated filters have been built from the theoretical analysis for experiment verifications.

II. Improved Integrated Models of EMI Filters

FMLFs are composed of properly arranged insulating layers, conductive layers and dielectric layers. Fig. 2 presents the commonly used single-strip FMLFs (with one dielectric layer), which can be regarded as the fundamental structure of FMLFs. Through different electrical configurations of the conductive layers and appropriate terminal activating mode, the FMLFs-based winding can reach various combinations of inductors and capacitors with different performance. As shown in Fig. 3, there are two commonly applied activating modes: CN-1 and CN-2, which have been reported in [21]. A line inductor and a CM capacitor can be integrated under CN-1 mode. While, in CN-2 mode, both CM inductor and DM capacitor can be integrated.

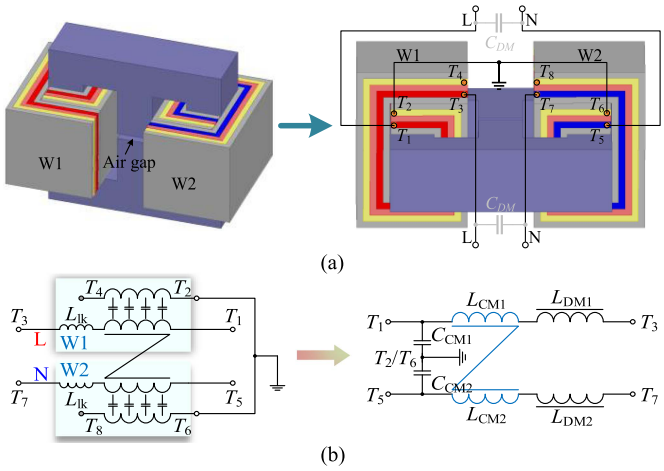

Fig. 4. Proposed modified FMLFs based CM choke with EE-type core. (a) Structure. (b) Lumped equivalent filtering circuit of the structure.

Utilizing the basic FMLFs shown in Fig. 3 or their derivative structures is enough for design of an EMI filter. Two single-strip FMLFs based windings in CN-1 activating mode are employed in [17] with an UU-core for a CM choke design, the integrated unit mainly integrates the CM inductor and CM capacitors. In this structure, the leakage path of CM windings is only provided by the surrounding air. Although the leakage is intended to be used as DM inductances, it is generally small and difficult to be controlled in practical design. Furthermore, Jiang et al. [23] have developed a fully integrated EMI filter with two modified multi-strip FMLFs-based windings in CN-2 activating mode. Compared to the CM choke model in [17], it extra integrates the DM capacitors and DM inductor. But, it can be seen that the DM inductance is only generated by the extended winding in one of the power lines, in this way, the structure is asymmetrical with respect to *L*- and *N*-lines. According to the analyses in [24], this circuit will make the impedances unbalanced in *L*- and *N*-lines, which will lead to a conversion from CM noise to DM noise.

In order to develop a modified systematic design method for EMI filters that frequently utilized in engineering practices, in this article, two ameliorative integrated structures are designed with FMLFs-based EMITs considering the common application scenarios. Instead of UU-cores, EE-cores are used for providing more creative space. Fig. 4 presents the recommended structure of a CM choke, two symmetrical single-strip FMLF windings (*W*1 and *W*2) are convolved on side legs of the core in CN-1 activating mode. The terminal ($T_1 \sim T_8$) configuration is depicted in Fig. 4(a), which is aimed at producing the CM inductance and CM capacitances. Furthermore, the central leg can serve as a leakage path with relatively low reluctance to raise the leakage inductances of CM windings. In this way, DM inductances that provided by the leakage inductances can be controlled through regulating length of the air gap in the central leg. The lumped equivalent topology of this electromagnetically integrated CM choke is presented in Fig. 4(b), which contains the CM and DM inductances, and CM capacitances. In the circuit, L_{CM1} (C_{CM1}, L_{DM1}) and L_{CM2} (C_{CM2}, L_{DM2}) stand for the CM inductances (CM capacitances, DM inductances) generated by *W*1 and *W*2,

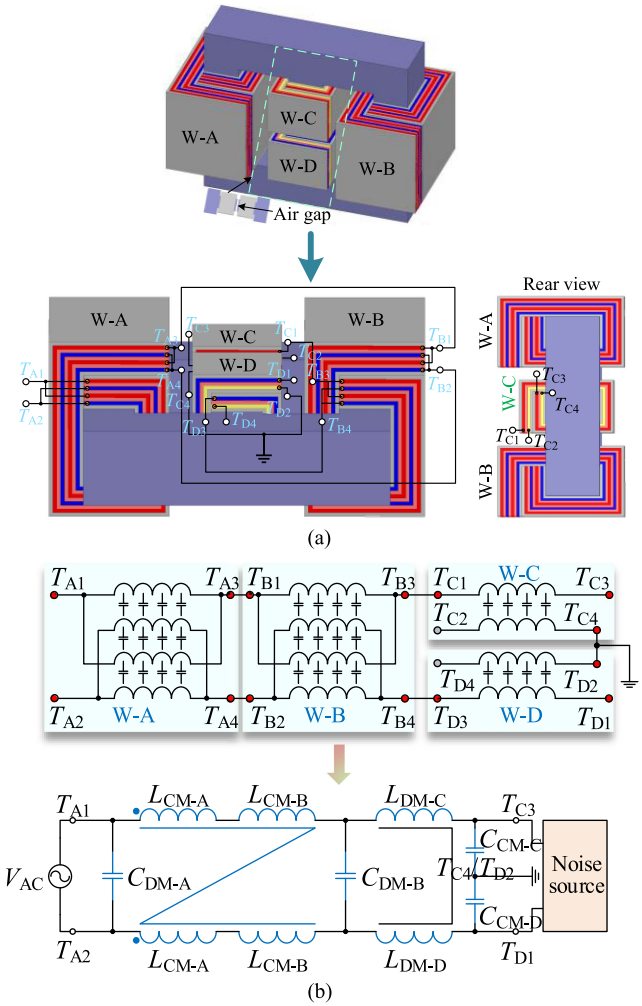

Fig. 5. Designed FMLFs based EMI choke with EE-type core. (a) Structure. (b) Lumped equivalent filtering circuit of the structure.

respectively. Moreover, as illustrated in Fig. 5(a), a complete electromagnetically integrated EMI filter is further designed for achieving both high CM and DM attenuation. Two symmetrical multi-strip FMLF windings (*W*–*A* and *W*–*B*) are rolled on side legs under CN-2 activating state for integrating CM inductors and DM capacitors. It should be noted that multistrip FMLFs are more suitable for integration of greater capacitances, such as DM capacitances. In addition, two symmetrical single-strip FMLFs windings (*W*–*C* and *W*–*D*) are convolved on the upper and lower central legs in CN-1 activating mode, which aim to generate DM inductances and CM capacitances with such port configuration. The lumped equivalent circuit of this integrated structure is shown in Fig. 5(b), where $L_{\mathrm{CM}\text{-}A}$ ($C_{\mathrm{DM}\text{-}A}$) and $L_{\mathrm{CM}\text{-}B}$ ($C_{\mathrm{DM}\text{-}B}$) are the CM inductances (DM capacitances) formed by *W*–*A* and *W*–*B*, respectively; $L_{\mathrm{DM}\text{-}C}$ ($C_{\mathrm{CM}\text{-}C}$) and $L_{\mathrm{DM}\text{-}D}$ ($C_{\mathrm{CM}\text{-}D}$) stand for the DM inductances (CM capacitances) generated by *W*–*C* and *W*–*D*, respectively. Obviously, a symmetrical filter can be constructed with integration of all the CM and DM filtering components in this way. It is worth mentioning that compared to the proposed CM choke, the EMI filter is much more difficult to be fabricated though it has a greater potential to achieve high

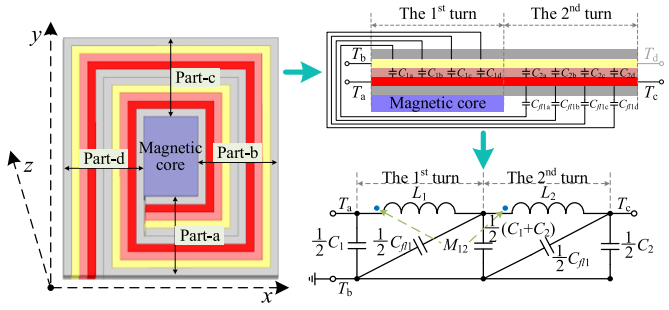

Fig. 6. Outspread description of a two-turn FMLFs based *W*1 (or *W*2).

DM attenuation. From the perspective of engineering practices, the designed CM choke and EMI filter are recommended as the preferable candidates for applications with relatively low and high DM attenuation requirements, respectively.

III. Analysis of the Integrated Models

For a specific design of the electromagnetic integrated EMI filter in a practical application, detailed performance analysis of the proposed structures is required. In this section, distributed electromagnetic circuit models (DEMCMs) of the designed CM and EMI chokes are discussed for a perspicuous presentation. Moreover, the magnetic coupling characteristics are analyzed based on the equivalent magnetic circuits. The realized CM and DM filtering topologies can be simplified, then the lumped filtering parameters can be defined according to the analyses.

A. DEMCMs of the Designed CM and EMI Chokes

The analysis begins with two-turn FMLF windings. Since the winding is a two-dimensional (3-D) structure, the parameters are assumed to be evenly distributed along the direction of *z*-axis. Therefore, the winding structure can be analyzed in a 2-D system for a more intuitionistic presentation. As shown in Fig. 6, when the FMLFs are wound on a magnetic core, both distributed inductances and capacitances are obtained at the same time. In addition, in a multiturn single-strip FMLF winding, stray capacitors will be produced between any two adjacent winding turns through the insulating layer, which are called flying capacitances here.

The top-right figure in Fig. 6 presents the outspread structure of a two-turn FMLFs based single-strip winding, where $C_{1(a\sim d)}$ and $C_{2(a\sim d)}$ represent the distributed capacitances of the first and second turns in Part-(*a*–*d*), respectively; $C_{fl1(a\sim d)}$ stand for the flying capacitances between the first and second turn windings in Part-(*a*–*d*). Taking each turn as a subunit, the distributed model of a two-turn *W*1 (or *W*2) can be depicted as a cascade structure with two identical subunits that composed of capacitances and coupled inductances. As shown in the bottom-right figure in Fig. 6, C_1 (or L_1) and C_2 (or L_2) stand for the equivalent capacitances (or inductances) generated by the first and second turn windings, respectively; C_{fl1} denotes the flying capacitor formed between the first and second turn windings through the insulating layer. In this way, DEMCM of *W*1 (similar to *W*2) is depicted in Fig. 7(a), then the DEMCM of the whole designed CM choke

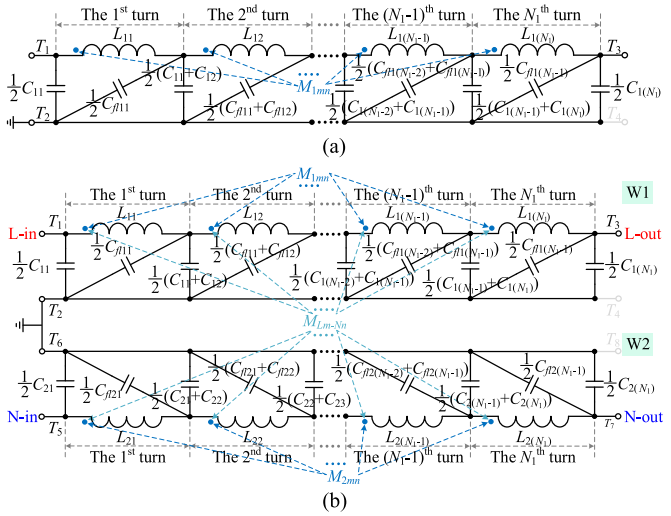

Fig. 7. DEMCMs of the designed CM choke. (a) Example with *W*1.(b) Whole model with *W*1 and *W*2.

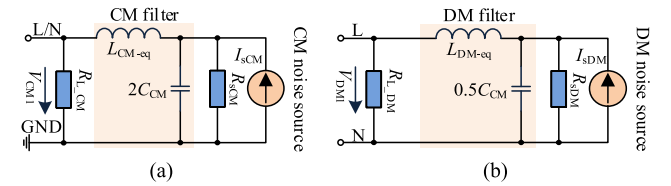

Fig. 8. Equivalent CM and DM lumped filtering circuits of the designed CM choke. (a) Common-mode, and (b) DM circuits.

can be described, as shown in Fig. 7(b). In the structure, *W*1 and *W*2 are symmetrically designed, the turn numbers of *W*1 (N_1) and W2 (N_2) are equal. $C_{1(1\sim N_1)}$ and $L_{1(1\sim N_1)}$ denote the distributed capacitors and inductors of the (1st$\sim N_1$th) turn winding of *W*1; $C_{fl1(1\sim(N_1-1))}$ represent the flying capacitors between the *i*th and (*i*+1)th turn windings ($i = 1, 2, 3 \ldots N_1$-1). Analogously, $C_{2(1\sim N_1)}$, $L_{2(1\sim N_1)}$ and $C_{fl2(1\sim(N_1-1))}$ stand for the corresponding distributed components and flying capacitors of W2. It can be seen that the flying capacitors are distributed between the power line and GND, which exist in CM in the circuit. In addition, M_{1mn} (or M_{2mn}) is the mutual inductance between the *m*th and *n*th turn windings of *W*1 (or *W*2), *m, n* = 1, 2, 3 …N_1; $M_{Lm\text{-}Nn}$ denotes the mutual inductance between the *m*th turn winding of *W*1 and the *n*th turn winding of *W*2. It is worth mentioning that the magnetic coupling between *L*- and *N*-line windings, which has a significant impact on the achieved DM inductances is not full coupling. The coupling is related to the core parameters and air gap design, detailed analyses will be presented in the following section. According to [17], the lumped CM and DM filtering circuits are presented in Fig. 8(a) and (b), respectively, where $L_{\text{CM-eq}}$ and $L_{\text{DM-eq}}$ are respectively the equivalent CM and DM (leakage) inductances; $C_{\text{CM}} = C_{\text{CM1}} = C_{\text{CM2}}$; $I_{s\text{CM}}$ and $R_{s\text{CM}}$ ($I_{s\text{DM}}$ and $R_{s\text{DM}}$) together stand for the CM (DM) noise source; R_{L_CM} and R_{L_DM} stand for the equivalent CM and DM impedances, respectively, of the line impedance stabilization network (LISN). From Fig. 8, CM and DM ILs of the CM choke can be derived from (1) with the

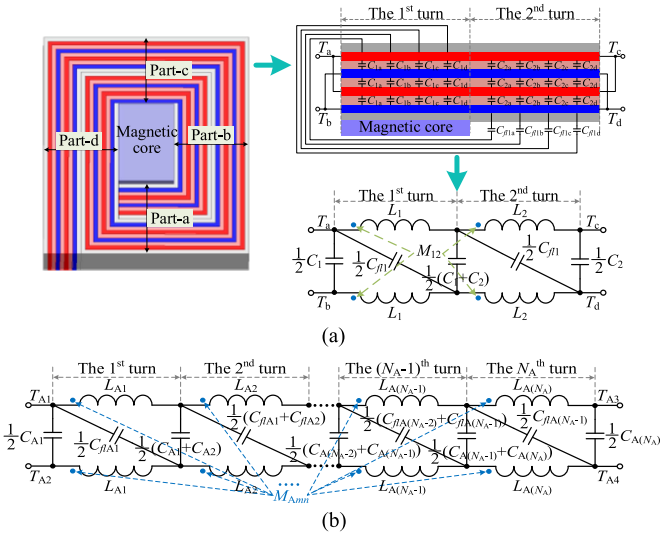

Fig. 9. (a) Outspread description of a two-turn FMLFs based *W–A* (or *W–B*). (b) DEMCM example with *W–A*.

noise source impedances R_{sCM} and R_{sDM} assumed as infinite. In [17] and [18], a node-analysis method is utilized based on the DEMCM, which indicates an approximate consistency of the predicted ILs with the DEMCM and lumped circuit, especially in relatively low-frequency range

$$\begin{cases} G_{\mathrm{CM1}} = 2L_{\mathrm{CM-eq}}C_{\mathrm{CM}}s^2 + 2R_{L\_\mathrm{CM}}C_{\mathrm{CM}}s + 1 \\ G_{\mathrm{DM1}} = 0.5L_{\mathrm{DM-eq}}C_{\mathrm{CM}}s^2 + 0.5R_{L\_\mathrm{DM}}C_{\mathrm{CM}}s + 1 \end{cases}. \quad (1)$$

Regarding to the designed EMI choke, there are some pivotal differences from the CM choke. The top-right figure in Fig. 9(a) shows the outspread structure of a two-turn multistrip FMLF winding in CN-2 activating mode. It can be seen that compared to the single-strip FMLF winding of the same length in CN-1 activating mode, this type of winding can realize a full coupled CM inductor, meanwhile, triple the distributed DM capacitance. The corresponding DEMCM is presented in the bottom-right figure in Fig. 9(a), as an expanded example, the DEMCM of *W–A* (or *W–B*) is depicted in Fig. 9(b). Moreover, the structure of *W–C* (or *W–D*) is similar to that of *W*1 (or *W*2), which can be depicted referring to the former presentation. Based on this, DEMCM of the designed EMI choke is presented in Fig. 10, where N_A and N_B stand for the turn numbers of *W–A* (or *W–B*) and *W–C* (or *W–D*), respectively; $C_{A(1\sim N_\mathrm{A})}$ ($C_{B(1\sim N_A)}$, $C_{C(1\sim N_B)}$, or $C_{D(1\sim N_B)}$) denote the distributed capacitors of the corresponding turn winding of *W–A* (*W–B*, *W–C*, or *W–D*); $L_{A(1\sim N_A)}$ ($L_{B(1\sim N_A)}$, $L_{C(1\sim N_B)}$ or $L_{D(1\sim N_B)}$) are the distributed inductors; $C_{flA(1\sim(N_A-1))}$ and $C_{flB(1\sim(N_A-1))}$ represent the flying capacitors in *W–A* and *W–B*, which exist in DM, different from this, the flying capacitors in *W–C* and *W–D* ($C_{flC(1\sim(\mathrm{N_B}-1))}$ and $C_{flD(1\sim(N_B-1))}$) exist in CM; M_{Ajk} (M_{Bjk}, $M_{Cpq,}$ or M_{Dpq}) is the mutual inductance between the *j*th and *k*th (or the *p*th and *q*th) turn windings of *W–A* (*W–B*, *W–C*, or *W–D*), $j, k = 1, 2, 3 \ldots N_\mathrm{A}$, $p, q = 1, 2, 3 \ldots N_B$; $M_{Aj\text{-}Bk}$ (or $M_{Cp\text{-}Dq}$) denotes the mutual inductance between the *j*th (or *p*th) turn winding of *W–A* (or *W–C*) and the *k*th (or *q*th) turn winding of *W–B* (or *W–D*). In this structure, it is desired to achieve full coupling between *W–A* and *W–B*, *W–C* and *W–D*, meanwhile, realizing function-decoupling between *W–A* (or *W–B*) and *W–C* (or *W–D*) through proper design of the EE-core and FMLF windings. If so, the EMI choke can obtain structure-integrated function-decoupled CM and DM filters. It means only the CM elements operate under CM excitations, and only the DM elements take effect under DM excitations. The lumped equivalent CM and DM filtering circuits are shown in Fig. 11(a) and (b), respectively, where $C^*_{\mathrm{CM}} = C_{\mathrm{CM}\text{-}C} = C_{\mathrm{CM}\text{-}D}$, $C_{\mathrm{DM}} = C_{\mathrm{DM\text{-}A}} = C_{\mathrm{DM}\text{-}B}$; $L^*_{\mathrm{CM-eq}}$ and $L^*_{\mathrm{DM-eq}}$ are the realized equivalent CM and DM inductances, respectively. Compared to the CM choke, it can be observed that the EMI choke has independent symmetrical DM inductances and capacitances, which makes it has a great potential to increase DM noise attenuation. The CM and DM ILs can be derived from

$$\begin{cases} G_{\mathrm{CM2}} = 2L^*_{\mathrm{CM-eq}}C_{\mathrm{CM}}s^2 + 2R_{L\_\mathrm{CM}}C^*_{\mathrm{CM}}s + 1 \\ G_{\mathrm{DM2}} = L^*_{\mathrm{DM-eq}}C_{\mathrm{DM}}C^*_{\mathrm{CM}}R_{L\_\mathrm{DM}}s^3 + 0.5L^*_{\mathrm{DM-eq}}C^*_{\mathrm{CM}}s^2 \\ \quad +R_{L\_\mathrm{DM}}\left(2C_{\mathrm{DM}} + C^*_{\mathrm{CM}}\right)s + 1. \end{cases} \quad (2)$$

B. Magnetic Coupling Analysis

Magnetic coupling characteristics of the windings are closely involved with filtering parameters of the EMI chokes, thus they are important factors which should be considered during the design procedure.

Fig. 12 shows the equivalent magnetic circuits of the EE-core based CM choke, where R_s, R_c, and R_{cg} stand for the reluctances of the upper or lower side leg (containing the yoke), the central leg, and the air-gap of the EE-core, respectively; l_g denotes the air-gap length. As depicted in Fig. 12(a), under CM excitations, there is a positive coupling between $\Phi_{W1\text{-CM}}$ and $\Phi_{W2\text{-CM1}}$ (or $\Phi_{W2\text{-CM}}$ and $\Phi_{W1\text{-CM1}}$). The coupling coefficient is related to the ratio of $\Phi_{W1\text{-CM1}}$ to $\Phi_{W1\text{-CM2}}$ (or $\Phi_{W2\text{-CM1}}$ to $\Phi_{W2\text{-CM2}}$), which is determined by l_g with a preselected EE-core. In contrast, the coupling between $\Phi_{W1\text{-DM}}$ and $\Phi_{W2\text{-DM1}}$ (or $\Phi_{W2\text{-DM}}$ and $\Phi_{W1\text{-DM1}}$) is negative under DM excitations, the coupling coefficient thereby will significantly influence the leakage inductance, as shown in Fig. 12(b). Where $\Phi_{W1\text{-CM}}$ ($\Phi_{W1\text{-DM}}$), $\Phi_{W1\text{-CM1}}$ ($\Phi_{W1\text{-DM1}}$) and $\Phi_{W1\text{-CM2}}$ ($\Phi_{W1\text{-DM2}}$) represent the fluxes of the primary branch, side leg branch, and central leg branch, respectively, produced by *W*1 under CM (DM) excitations; $\Phi_{W2\text{-CM}}$ ($\Phi_{W2\text{-DM}}$), $\Phi_{W2\text{-CM1}}$ ($\Phi_{W2\text{-DM1}}$) and $\Phi_{W2\text{-CM2}}$ ($\Phi_{W2\text{-DM2}}$) are the relevant branch-fluxes formed by *W*2 under CM (DM) excitations. From the analyses above, it is required to identify and regulate the coupling coefficient for reasonable parameter design. Due to the symmetry of this structure, a simplified magnetic circuit can be used for the analysis, as shown in Fig. 12(c), where the fluxes of the primary branch (Φ_{W1}), side leg branch (Φ_{W11}), and central leg branch (Φ_{W12}) meet

$$\Phi_{W1} = \frac{N_1 I}{R_{si}} = \Phi_{W11} + \Phi_{W12}. \quad (3)$$

The reluctances of self-inductance (L_{si1}) of each winding and mutual inductance (L_{mi1}) between the two windings are derived as (4). The equivalent branch reluctances R_1 and R_2 can

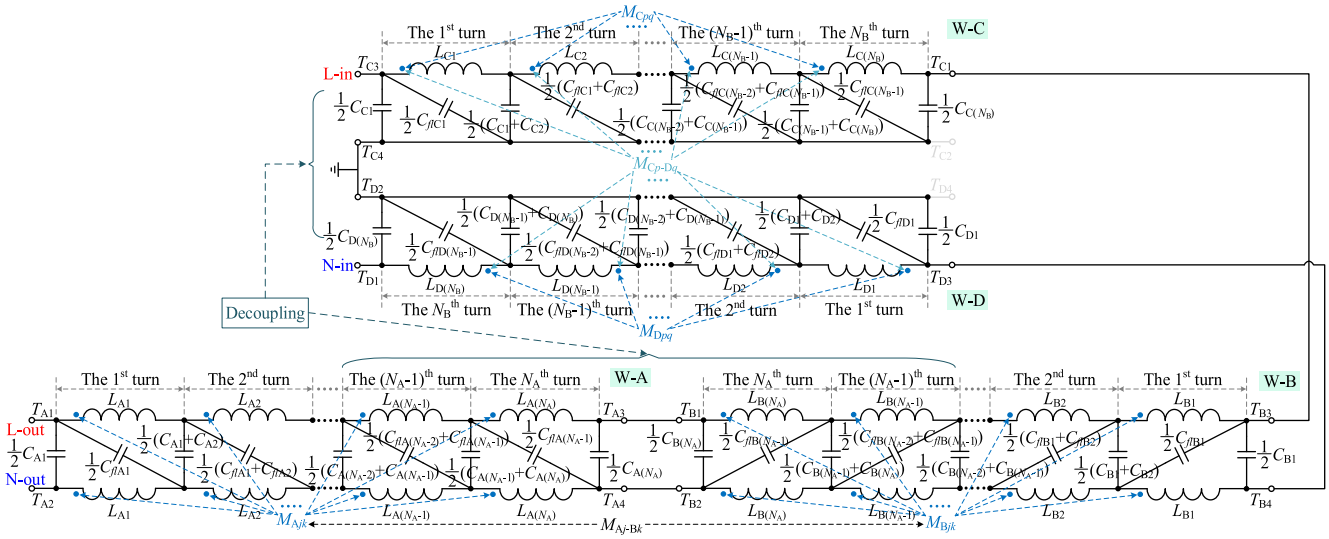

Fig. 10. DEMCM of the designed EMI choke.

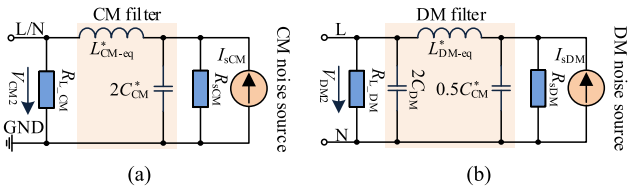

Fig. 11. Equivalent CM and DM lumped filtering circuits of the designed EMI choke. (a) CM, and (b) DM circuits.

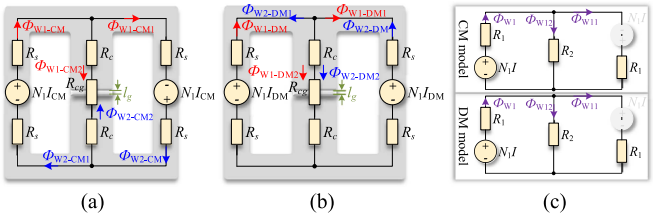

Fig. 12. Equivalent magnetic circuits of the designed CM choke. (a) Under CM excitations, (b) Under DM excitations, and (c) Simplified circuit for coupling analysis.

be estimated from (5), where l_s, l_y, and l_c denote the lengths of side leg, yoke and central leg, respectively, of the core; A_s, A_y, and A_c represent the corresponding cross-sectional areas; μ_0 stands for the permeability of vacuum ($\mu_0 = 4\pi \times 10^{-7}$H/m), and μ_r denotes the core's relative permeability. According to (4), the coupling coefficient k_{m1} can be expressed as (6)

$$\begin{cases} R_{si1} = R_1 + R_1//R_2 = R_1 + \frac{R_1 R_2}{R_1+R_2} \\ R_{mi1} = \frac{N_1 I}{\Phi_{W11}} = \frac{N_1 I}{\Phi_{W1} \cdot \frac{R_2}{R_1+R_2}} = \frac{R_1+R_2}{R_2} \cdot R_{si} \end{cases} \tag{4}$$

$$\begin{cases} R_1 = 2R_s = 2 \times \left(\frac{l_s}{\mu_0 \mu_r A_s} + \frac{l_y}{\mu_0 \mu_r A_y} \right) \\ R_2 = 2R_c + R_{cg} = 2 \times \frac{l_c}{\mu_0 \mu_r A_c} + \frac{l_g}{\mu_0 A_c} \end{cases} \tag{5}$$

$$k_{m1} = \frac{R_{si1}}{R_{mi1}} = \frac{R_2}{R_1 + R_2}. \tag{6}$$

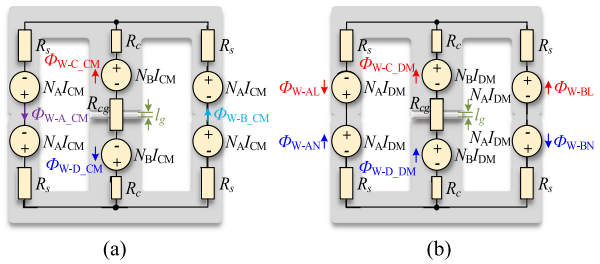

Fig. 13. Equivalent magnetic circuits of the designed EMI choke. (a) Under CM excitations. (b) Under DM excitations.

Under CM excitations, the magnetic coupling status between the windings on side-legs (*W–A* and *W–B*) of the EMI choke is similar to that of the CM choke, the expression of coupling coefficient (k_{m2}) between *W–A* and *W–B* is equal to k_{m1}. But as shown in Fig. 13, it is worth mentioning that the interleaved multi-layer structure and the terminal configuration (CN-2) will multiply the self and mutual inductances of *W–A* and *W–B*. However, under DM excitations, there is a great difference, as indicated in Fig. 13(b), the magnetic fluxes produced by *L*-layer and *N*-layer of the winding will counteract each other. Thus, the effective leakages will be significantly reduced, so their impacts can be neglected in this model. Regarding to *W–C* and *W–D*, the performance is just the opposite. The fluxes generated by *W–C* and *W–D* will counteract each other under CM excitations, and will strengthen each other under DM excitations. There is a full coupling (coupling coefficient $k_{m3} = 1$) between *W–C* and *W–D*, reluctances of the self- and mutual inductances (L_{si2} and L_{mi2}) are equal, which can be derived as (7). In addition, as has been discussed above, CM windings (*W–A*, *W–B*) and DM windings (*W–C*, *W–D*) are function-decoupled, this feature can simplify the CM and DM filtering circuits for parameter design

$$R_{si2} = R_{mi2} = R_2 + R_1//R_1 = R_s + 2R_c + R_{cg}. \tag{7}$$

IV. Specification Determination

Definitions and considerations of technical specifications of the CM and EMI chokes are the basics for reasonable design. In this part, the determinations of inductances and capacitances involved with the chokes' parameters are presented first as the main guidance. Moreover, some important indexes such as flux density, current density, voltage range, and core window utility are analyzed and considered with proper limitations.

A. Lumped CM and DM Filtering Components

1) CM and DM Inductances:

a) The CM choke: From the magnetic analyses in Section III, the CM and DM inductances of the CM choke can be expressed as (8) and (9), respectively. It can be observed that although the coupling coefficient k_{m1} has a great impact on the coupling strength between the two windings, but it will not influence the lumped equivalent CM inductance. While, the greater k_{m1} is, the smaller $L_{\text{DM-eq}}$ will be. Thus, k_{m1} can be regulated appropriately to meet the DM inductance for fully satisfying the requirements

$$\begin{aligned} L_{\text{CM-eq}} &= L_{\text{CM\_}L}//L_{\text{CM\_}N} = \frac{1}{2}\left(L_{si1}+L_{mi1}\right) \\ &= \frac{1}{2}\left(N_1\cdot\frac{\boldsymbol{\Phi}_{W1-\text{CM}}+\boldsymbol{\Phi}_{W2-\text{CM1}}}{I_{\text{CM}}}\right) \\ &= \frac{1}{2}\left(\frac{N_1^2}{R_{si1}}+\frac{N_1^2}{R_{mi1}}\right) = \frac{1}{2}\left(1+k_{m1}\right)\cdot\frac{N_1^2}{R_{si1}} = \frac{N_1^2}{2R_1} \end{aligned} \tag{8}$$

$$\begin{aligned} L_{\text{DM-eq}} &= L_{lk\_L}+L_{lk\_N} \\ &= N_1\cdot\frac{\boldsymbol{\Phi}_{W1-\text{DM2}}+\boldsymbol{\Phi}_{W2-\text{DM2}}}{I_{\text{DM}}} = 2(1-k_{m1})\cdot\frac{N_1^2}{R_{si1}}. \end{aligned} \tag{9}$$

b) EMI choke: Compared to the CM choke, both self and mutual inductances of *W–A* and *W–B* will be multiplied due to the multi-strip winding structure with interleaved *L*- and *N*-layers. As shown in (10), it can be seen that if both the CM and EMI chokes are designed with the same type of core, the EMI choke can halve the required turn number

$$\begin{aligned} L^*_{\text{CM-eq}} &= L_{\text{CM\_}L}//L_{\text{CM\_}N} = \frac{1}{2}\left(L_{si2}+L_{mi2}\right) \\ &= \frac{1}{2}\left(2N_A\cdot\frac{\boldsymbol{\Phi}_{W-A\_\text{CM}}+\boldsymbol{\Phi}_{W-B\_\text{CM1}}}{I_{\text{CM}}}\right) \\ &= \frac{1}{2}\left(\frac{4N_A^2}{R_{si1}}+\frac{4N_A^2}{R_{mi1}}\right) = 2\left(1+k_{m2}\right)\cdot\frac{N_A^2}{R_{si1}} = \frac{2N_A^2}{R_1}. \end{aligned} \tag{10}$$

In addition, as derived in (11), different from the CM choke, the lumped DM inductance of the EMI choke will not directly affected by the coupling coefficient between *W–A* and *W–B*, which is only involved with *W–C's* (or *W–D's*) turn number and its self-inductive reluctance. For CM inductor, the greater k_{m2}, the higher the coupling degree. But actually, greater k_{m2} means larger air gap, which will increase the required turn-numbers of

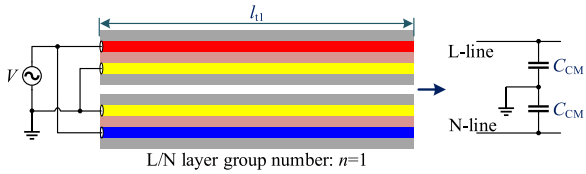

Fig. 14. Formation diagram of CM capacitators in the CM choke.

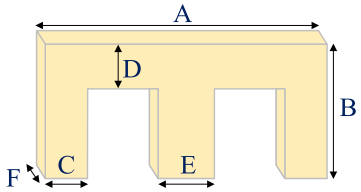

Fig. 15. Specifications of the magnetic core.

W–C and *W–D*. For this reason, k_{m2} also needs to be reasonably selected according to the expected DM inductances and limited flux density

$$\begin{aligned} L^*_{\text{DM-eq}} &= L_{\text{DM\_}L}+L_{\text{DM\_}N} \\ &= 2\left(N_B\cdot\frac{\boldsymbol{\Phi}_{W-C\_\text{DM}}+\boldsymbol{\Phi}_{W-D\_\text{DM}}}{I_{\text{DM}}}\right) \\ &= 2\left[N_B\cdot\left(\frac{N_B I_{\text{DM}}}{R_{si2}I_{\text{DM}}}+\frac{N_B I_{\text{DM}}}{R_{mi2}I_{\text{DM}}}\right)\right] = \frac{4N_B^2}{R_{\text{si2}}}. \end{aligned} \tag{11}$$

2) CM and DM Capacitances: It should be noted that flying capacitances are much smaller than the dominant CM and DM capacitances, owing to much greater thickness and lower permittivity of the insulating layers. Therefore, they are neglected during the design procedure.

a) CM choke: The formation of CM capacitors is simply described in Fig. 14, then, the achieved CM capacitance can be defined from (12), where ε_0 denotes the vacuum permittivity ($\varepsilon_0 = 8.85\times10^{-12}$F/m), ε_r represents the relative permittivity of dielectric layer; n is the group number of *L/N* layers; d_d is the thickness of the dielectric layers; and l_{1G} and w_{1G} are the length and width of GND-layer, respectively, in *W*1 (or *W*2). In this model, no independent DM capacitor is integrated, the equivalent DM capacitance is only provided by the CM capacitors operating in differential mode. Hence, $C_{\text{DM-eq}} = 0.5C_{\text{CM}}$

$$\begin{cases} C_{\text{CM}} = \frac{\varepsilon_r\varepsilon_0 A_{1G}}{d_d} = (2n-1)\cdot\frac{\varepsilon_r\varepsilon_0 l_{1G}w_{1G}}{d_d} = \frac{\varepsilon_r\varepsilon_0 l_{1G}w_{1G}}{d_d} \\ C_{\text{DM-eq}} = 0.5C_{\text{CM}} \end{cases}. \tag{12}$$

Moreover, it should be noted that the maximum of $l_{1\text{G}}$ should be no more than the total length (l_{t1}) of *W*1 (or *W*2), l_{1G} can be regulated within l_{t1} according to the expected CM capacitance. l_{t1} evolves nonlinearly with the turn number, it can be estimated from (13), where $l_1(N)$ is perimeter of the *N*th turn winding of W1; *C* and *F* stands for the side-leg size of the core, as presented in Fig. 15; d_i and d_e denote the thicknesses of insulating and

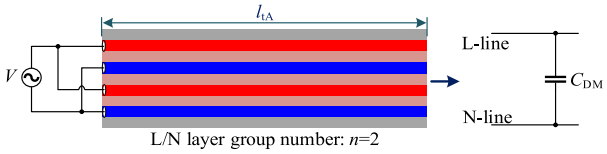

Fig. 16. Formation diagram of DM capacitators in the EMI choke.

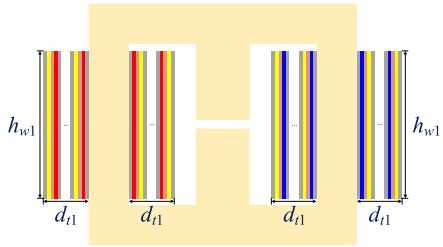

Fig. 17. Sectional view of the CM choke.

electrical layers, respectively,

$$l_{t1} = \sum_{N=1}^{N_1} l_1(N) \approx 2 \times \sum_{N=1}^{N_1} \times [C + F + 4(N-1)(2d_i + 2d_e + d_d)]. \quad (13)$$

b) EMI choke: The formation principle of CM capacitors in the EMI choke is the same as that of the CM choke, the lumped CM capacitances can be determined from a similar formula. As given in (14), where l_{CG} and w_{CG}, respectively, represent the total length and width of the GND-layer in *W–C* (or *W–D*). l_{CG} should be adjusted within the total length (l_{tC}) of *W–C* (or *W–D*). Fig. 16 illustrates the formation principle of the DM capacitor, according to which the DM capacitance can be defined from (15), where l_{tA} and w_{Ae} stand for the total length, and electrical-layer width, respectively, of *W–A* (or *W–B*)

$$C^*_{CM} = \frac{\varepsilon_r \varepsilon_0 A_{CG}}{d_d} = \frac{\varepsilon_r \varepsilon_0 l_{CG} w_{CG}}{d_d} \quad (14)$$

$$C_{DM} = (2n-1) \cdot \frac{\varepsilon_r \varepsilon_0 l_{tA} w_{Ae}}{d_d} = 3 \times \frac{\varepsilon_r \varepsilon_0 l_{tA} w_{Ae}}{d_d}. \quad (15)$$

Similar to l_{t1}, l_{tC}, and l_{tA} can be estimated from (16), where $l_C(N)$ and $l_A(N)$ denote perimeters of the *N*th turn winding of *W–C* and *W–A*, respectively; *E* represents the width of central leg of the magnetic core

$$\begin{cases} l_{tC} = \sum_{N=1}^{N_B} l_C(N) \approx 2 \times \sum_{N=1}^{N_B} \\ [E + F + 4(N-1)(2d_i + 2d_e + d_d)] \\ l_{tA} = \sum_{N=1}^{N_A} l_A(N) \approx 2 \times \sum_{N=1}^{N_A} \\ \times [C + F + 4(N-1)(2d_i + 4d_e + 3d_d)] \end{cases}. \quad (16)$$

B. Considerations of Performance Reliability

1) Current Density: Generally, the safe current carrying capacity of copper wire is 5–8 A/mm^2, for a reliable design, the current density is limited within 5 A/mm^2. Therefore, the size of the electrical layer needs to meet

$$\frac{I_{max}}{A_{et}} = \frac{I_{max}}{nA_e} = \frac{I_{max}}{nw_e d_e} \le 5\text{A/mm}^2 \quad (17)$$

where I_{max} is the maximum current that flows through the choke; A_{et} stands for total cross-sectional area of the *L/N* layers. Here, it is worth mentioning that the sizes of electrical layers of *W–A* (or *W–B*) and *W–C* (or *W–D*) of the EMI choke are better to be adjusted for attaining a unified current carrying capacity.

2) Breakdown Voltage: Breakdown voltage of the dielectric materials is a constraint for the thickness-range of dielectric layers, which requires

$$d_{d-req} > \frac{V_{max}}{E_b(V/\mu m)} \quad (18)$$

where V_{max} denotes the maximum voltage across the integrated capacitor, and E_b represents breakdown field strength of the dielectric materials.

3) Flux Density: Because CM currents are relatively small (on mA level) and only part of them constitute excitations, generally, they will not result in saturation of the core. Hence, flux density under the excitation of fundamental current in a converter is the main consideration for antisaturation design. Under this excitation, there will be a lot of fluxes passing through central leg of the core. From the analyses above, (19) and (20) need to be met in the designed CM and EMI chokes, respectively,

$$B_{sat} \ge \frac{\Phi_{W1-DM2\_max} + \Phi_{W2-DM2\_max}}{A_c} = 2 \times \frac{N_1 I_{max}}{R_{si1} A_c} \cdot (1 - k_{m1}) \quad (19)$$

$$B_{sat} \ge \frac{\Phi_{W-C\_DM\_max} + \Phi_{W-D\_DM\_max}}{A_c} = 2 \times \frac{N_B I_{max}}{R_{si2} A_c}. \quad (20)$$

C. Window Utilization of the Core

On the other hand, suitability of the selected EE-type core size is another main factor for design of the proposed CM and EMI chokes. In this article, the expected utility ratios of the core window are limited above a preset level for the design. In order to facilitate quantitative analysis, two indexes: r_x and r_z (the utility ratios in *x*-axis and *z*-axis) are considered.

1) CM Choke: Fig. 17 shows the sectional view of the CM choke, it can be observed that r_{x1} and r_{z1} are relevant to total thickness (d_{t1}) and height (h_{w1}), respectively, of *W*1 (or *W*2). In order to take full advantage of the core window while reserving a space margin for the manufacture, the core window utilization is limited as

$$\begin{cases} 60\% \le r_{x1} = \frac{d_{t1}}{w_{Cx}} \approx \frac{N_1(2d_i + 2d_e + d_d)}{0.5 \times (A - 2C - E)} \times 100\% \le 90\% \\ 60\% \le r_{z1} = \frac{h_{w1}}{2 \times (B - D)} \times 100\% < 100\% \end{cases}. \quad (21)$$

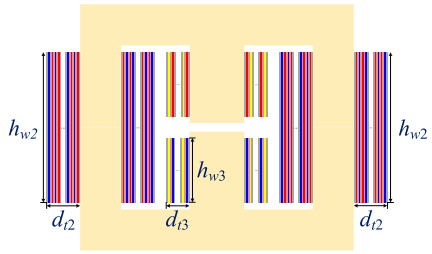

Fig. 18. Sectional view of the EMI choke.

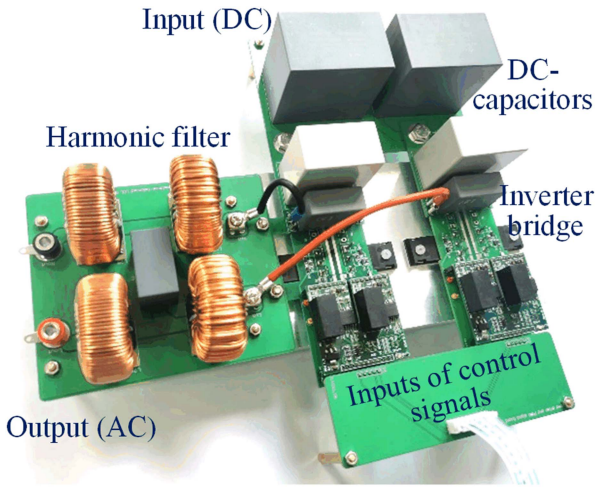

Fig. 19. Prototype of the targeted SiC-MOSFET based high-frequency converter platform.

2) EMI Choke: Fig. 18 shows the sectional view of the EMI choke, different from the CM choke, the windings designed on central leg need to be extra considered in the EMI choke. With expected window utilization similar to that of the CM choke, the utility ratio of the core window is limited as

$$\begin{cases} 60\% \le r_{xA} = \frac{d_{t2}+d_{t3}}{w_{Cx}} \\ \quad \approx \frac{N_A(2d_i+4d_e+3d_d)+N_B(2d_i+2d_e+d_d)}{0.5\times(A-2C-E)} \times 100\% \le 90\% \\ 60\% \le r_{zA} = \frac{h_{w2}}{2\times(B-D)} \times 100\% < 100\% \\ 60\% \le r_{zC} = \frac{2h_{w3}}{2\times(B-D)} \times 100\% < 100\% \end{cases} . \tag{22}$$

V. Practical Implementation

In this part, a unipolar frequency-doubling sinusoidal PWM controlled high-frequency SiC-MOSFET inverter is utilized as the experimental platform, as presented in Fig. 19, its technical specifications are given in Table I. To verify and discuss the performance of the recommended approach, prototypes of the proposed CM and EMI chokes are built for detailed analysis on some crucial indices. Both the chokes are constructed with the same type of magnetic core. Furthermore, in order to reflect the superiorities of the proposed structures, state-of-the-art filters investigated in [17] and [23] are built for comparisons.

TABLE I
Technical Specifications of the Inverter System

Description	Symbol	Value
DC-link voltage	V_{dc}	400 V
AC-side output voltage rms	V_{ac}	220 V
Output power	P_o	500 W
Fundamental frequency	f_0	50 Hz
Switching frequency	f_{sw}	100 kHz
Converter-side filtering inductance	L_1	2.5 mH
Grid-side filtering inductance	L_2	1.25 mH
Filtering capacitance	C_f	3.3 μF

TABLE II
Comparison Among Different Magnetic Materials

Relevant indices	Sendust	Ferrite (Mn-Zn)	Fe-based Amorphous	Nanocrystalline
Saturation flux density (T)	1.05	0.53	1.56	1.25
Initial relative permeability	26-125	1k-15k	3k-6k	15k-150k
Core loss (mW/cm^3)	+ +	+	+ + + +	+ + +
Operation temperature (°C)	150	250	150	120
Relative cost	+ +	+	+ + +	+ + + +

Symbols: Higher (+ + + +); high (+ + +); average (+ +); and low (+).

At present, there are some different types of core materials can be available on the market, mainly including Sendust (Fe-Si-Al), ferrite (Mn-Zn), amorphous materials, nanocrystalline, etc. Some key indices of the above core materials are given in Table II. From the flux saturation perspective, in general, the greater the permeability, the easier for the core to reach saturation. Hence, Sendust, ferrite, and Fe-based amorphous powder cores can be used in a wide power range. By contrast, nanocrystalline cores are only appropriate for design of CM inductors or low-power inductors, Sendust materials, which are commonly employed for DM inductor design, are not optimal for CM inductor due to their general low permeability. In this article, the design objectives contain both CM and DM elements, therefore, ferrite and Fe-based amorphous cores are the optional candidates. In addition, considering the inverter system's power level (500 W), core losses and costs, ferrite cores are utilized for the integration design.

In this article, the TDK PC95 series EE cores are utilized for design of the proposed improved integrated EMI filters due to their balanceable permeability ($\mu_r = 3300$ at 25 °C and 100 kHz) and saturation flux density ($B_{\rm sat} = 530$ mT at 25 °C and 480 mT at 60 °C). According to the expected parameter design objectives that determined based on the noise attenuation requirements, the specification of the EE core is selected to be 55/28/21 from the design principles and constraints presented in Section IV, as illustrated in Fig. 20. With the core size and characteristic of the core permeability, the magnetic coupling coefficient between the two FMLF windings on the side legs (in the CM choke or EMI choke) can be estimated from (5) and (6), the correlation curve is depicted in Fig. 21. It should be noted that the relative permeability of the core can maintain a high level (3300–4000)

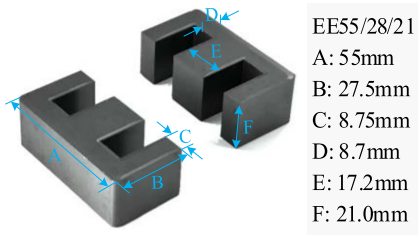

Fig. 20. Dimensions of the EE-type core with specification 55/28/21.

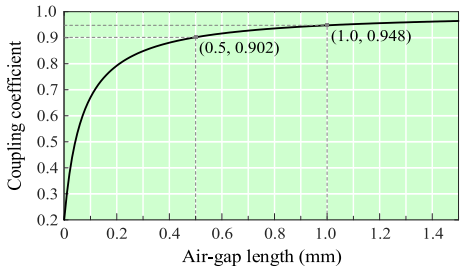

Fig. 21. Correlation curve between the coupling coefficient (k_{m1} or k_{m2}) and air-gap length in the center leg.

TABLE III
PARAMETERS OF THE DESIGNED CM AND EMI CHOKES

Parameters	Proposed CM choke	Proposed EMI filter	
	W1/W2	W–A/W–B	W–C/W–D
w_i	32 mm	32 mm	17 mm
w_e/w_G	30 mm	30 mm	15 mm
w_d	32 mm	32 mm	17 mm
d_i	0.1 mm	0.1 mm	0.1 mm
d_e/d_G	50 μm	25 μm	100 μm
d_d	12.5 μm	12.5 μm	12.5 μm
l_{1G}/l_{CG}	0.16 m	\	0.32 m
$N_1/N_A/N_B$	24	12	12
l_g	0.5 mm	1.0 mm	
$L_{CM\text{-}eq}$	2.4 mH	2.4 mH	
$L_{DM\text{-}eq}$	480 μH	240 μH	
C_{CM}	12 nF	12 nF	
C_{DM}	\	0.2 μF	

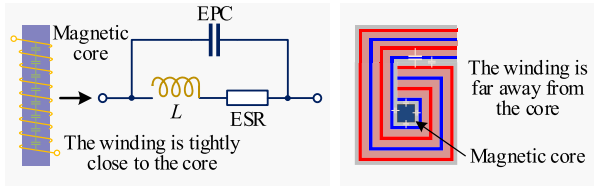

Fig. 22. Distribution diagrams of the parasitic capacitors in (a) common discrete inductor, and (b) FMLFs based integrated unit.

from 25 °C to 80 °C, and it is quite steady within 1 MHz. Hence, for providing a reference for sufficient design of the air-gap length, the correlation curve is fitted with $\mu_r = 3300$, It can be seen from Fig. 21 that the coupling coefficients are around 0.90 and 0.95 when the air gap lengths are set as 0.5 and 1.0 mm, respectively. In order to not significantly weaken the magnetic coupling between the two CM inductor windings (on side legs), the coupling coefficients are expected to be above 0.90 in both the filters. In the CM choke, with the aim of achieving greater leakage (DM) inductances, the expected coupling coefficient is 0.90. While in the EMI choke, the coupling coefficient has no significant impact on DM inductances. From the prospective of coupling strength of CM inductors and the flux density, the greater the air gap length, the better, but too large air gap will result in over consumption of DM inductor windings. For balancing these two aspects, the expected coupling coefficient in the EMI choke is set as 0.95.

As for the FMLF windings, their specific parameters need to be designed based on the preselected materials. Polyimide (PI) films, which have better comprehensive properties compared to other dielectric films on the market, are utilized as the dielectric layers. The relative permittivity (ε_r) and breakdown voltage of PI films are about 3.5 and 280 V/μm, respectively. In addition, red copper foils and high-temperature resisting Mylar tape are used as the conductive layers and insulating layers, respectively. In this article, the filtering parameters of the CM and EMI chokes are preselected using the method introduced in [9] with standard EN55011-class B referenced. For achieving expected filtering technical specifications, parameters of the FMLF windings that employed in the CM and EMI chokes are designed according to Section IV, as given in Table III. It should be noted as follows.

1) For preventing short-circuit, the employed dielectric layers are slightly wider than the associated conductive layers;
2) There are some specific differences in thicknesses of the FMLF windings with different structures or widths owing to the requirement for uniformity of current density.

In addition, parasitic parameters of the filtering components have great impacts on noise suppression ability of an EMI filter. Similar to discrete filters, parasitic parameters in FMLF-based filters are mainly the equivalent parallel capacitances (EPCs) of the filtering inductors and equivalent series inductances (ESLs) of the filtering capacitors. The EPCs will reduce the inductors' impedances and the ESLs will raise the capacitors' impedances, due to which the filter's EMI suppression performance will be weakened, particularly above self-resonance frequencies of the components. This issue cannot be thoroughly avoided, but can be alleviated through reasonable design. Compared to discrete filters, generation modes of parasitic parameters in the proposed filter have some differences. As depicted in Fig. 22(a), the EPCs in a discrete inductor constructed with common copper coils are mainly generated between adjacent turns of the winding, and between winding and the magnetic core. While in the integrated unit built with FMLF windings, as illustrated in Fig. 22(b), the coils are far away from the magnetic core due to the laminated structure. What's more, the electrical layers are shielded with insulating layers. Therefore, the parasitic capacitances relevant to the core can be markedly lessened in this structure. Turn-to-turn capacitances which are closely related to the insulating layers are dominant in the winding, they can be diminished by properly raising the thickness of the insulating layers or using

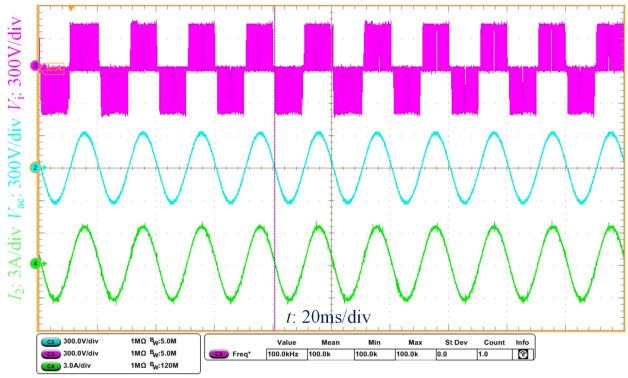

Fig. 23. Output voltage and current waveforms of the inverter system.

insulating materials with lower permittivity. This is the reason why the insulating layers are designed to be much thicker than the dielectric layers ($d_i = 0.10$ mm and $d_d = 12.5$ μm). As for the ESL in a capacitor, it is generally induced by residual inductors of the electrodes and leads. The ESL in a FMLF winding can be decreased by reasonably reducing lengths of the winding and terminal leads (the required winding length can be reduced by splitting the *L* and *N* layers into more groups).

Moreover, the used ferrite core type in design of the existing FMLF-based CM and EMI chokes is PC40 UU58/33/14, which is the same as the core type used in [23]. It needs to be noted that the existing CM choke has no independent DM inductances except for the quite small leakage inductances, thus, there is no definite dimension limitation regarding antisaturation design for its magnetic core. However, for the existing EMI choke, two pairs of the UU-type magnetic cores are required for preventing magnetic saturation. For this reason, two pairs of the UU-type cores are employed in both the aforesaid chokes for maintaining the consistent condition of CM filter design. In the existing CM and EMI chokes, the FMLF types and sizes are the same as those of *W*1 or *W*2 in the proposed CM choke and *W–A* or *W–B* in the proposed EMI choke, respectively. In order to achieve nearly the same filtering parameters, turn numbers of the CM inductor windings in the two chokes are 20 and 10, respectively. Lengths of the embedded GND layers in the chokes are both 0.16 m. Apart from the winding that embedded with GND layer, another winding in the existing EMI choke is designed with 6 turns of extended winding in *L*-layer, which is aimed to produce DM inductance. With such design, the realized CM inductances and CM capacitances of the chokes are both 2.36 mH and 12 nF, respectively. The DM inductance and DM capacitance of the existing EMI choke are 212.4 μH, and 214.4 nF, respectively.

A. Finite-Element Analysis

When the system is operating at rated power, the peak value of the output current is around 3.2 A, as shown in Fig. 23. Taking such current as excitation, flux distributions of the proposed CM choke and EMI choke are analyzed through finite-element method (FEM) simulation with ANSYS electromagnetics suite software. From Fig. 24(a), it can be observed that the equivalent magnetic fluxes generated by the windings on side legs of the

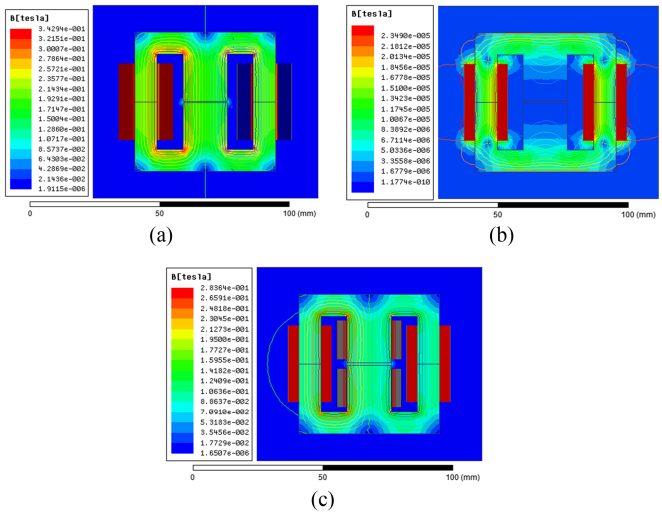

Fig. 24. Magnetic flux distributions in (a) proposed CM choke, (b) CM inductor windings in the EMI choke, and (c) whole proposed EMI choke.

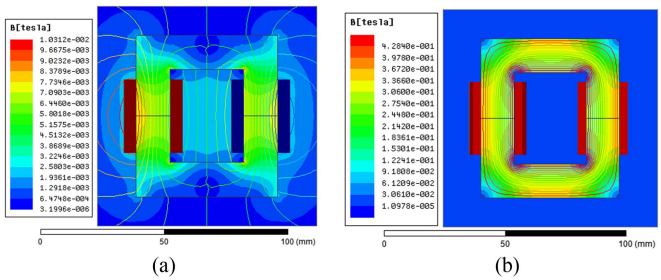

Fig. 25. Magnetic flux distributions in (a) existing CM choke, and (b) existing EMI choke.

CM choke are mainly the leakage fluxes that pass through the central leg. The fluxes in the central and side legs of the core are nearly evenly distributed since $A_c \approx 2A_s \approx 2A_y$, the average flux density is about 180 mT. In contrast, leakage fluxes from the CM inductor windings (*W–A* and *W–B*) in the EMI filter are much fewer due to the interleaved *L*/*N* layers. As shown in Fig. 24(b), the corresponding flux density that introduced by the leakage fluxes are less than 0.022 mT. After DM inductor windings (*W–C* and *W–D*) are configured, the magnetic fluxes introduced by them become dominated, as presented in Fig. 24(c), the average flux density is raised to about 90 mT. It is worth mentioning that the flux densities in the CM and EMI chokes are consistent with the theoretical calculations from (19) and (20), respectively. The magnetic cores in both chokes will not be saturated in such an application condition, this is a main precondition for getting satisfied filtering performance. Additionally, for comparative analyses, flux distributions of the existing CM and EMI chokes are simulated. As can be seen from Fig. 25(a), flux densities in the existing CM choke are quite low, which is normal since the magnetic fluxes generated by the two CM inductance windings under fundamental current excitation will counteract each other. However, as shown in Fig. 25(b), flux densities in the existing EMI choke are much higher because a DM inductance is extra integrated. From the comparison between Figs. 24(c) and 25(b),

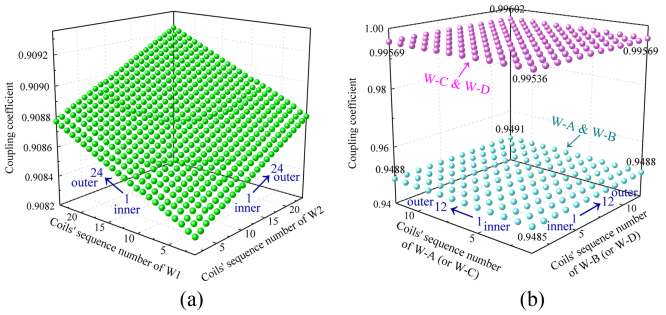

Fig. 26. FEM simulated magnetic coupling coefficients between any two associated windings in the (a) CM choke, and (b) EMI filter.

TABLE IV
SIZE AND WEIGHT COMPARISONS OF THE CM AND EMI CHOKES

Indices	Existing CM choke	Proposed CM choke	Existing EMI choke	Proposed EMI Choke
Weight (g)	403.5	384.7	426.7	382.6
Volume (cm^3)	107.3	80.14	113.6	78.16

it can be seen that the proposed EMI choke can markedly diminish the flux density, which indicates its superiority in filter size diminution and core loss reduction.

Fig. 26 presents the FEM simulated distributions of magnetic coupling coefficients between associated FMLF windings in the CM and EMI chokes. From Fig. 26(a), it can be seen that the coupling coefficients between the coils in *W*1 and *W*2 are in the range from 0.9082 up to 0.9093, they are approximately in line with the expected value (0.90). In the EMI filter, the state has some specific differences. As shown in Fig. 26(b), the coupling between *W–A* and *W–B* is nearly full, the relevant coefficients are tightly closed to the expected value (0.95). Moreover, *W–C* and *W–D* are fully coupled, the coupling coefficients are greater than 0.995. On the whole, the aforementioned analyses indicate the reasonability and feasibility of the design.

B. Measurements of Some Important Indices

According to the expected specifications given in Table III, prototypes of the proposed CM and EMI chokes are designed, as shown in Fig. 27(a) and (b), respectively. Some key indices of the two chokes are measured for performance analysis and discussions. Furthermore, as presented in Fig. 27(c) and (d), the existing counterparts are constructed for pertinent comparisons, which aims to reflect the superiority of the proposed method.

The weight and size comparisons among different types of CM and EMI chokes are given in Table IV, as can be seen, there are no remarkable differences between the two proposed chokes. It is worth mentioning that the proposed EMI choke has slight reductions in weight and size though extra DM capacitors are integrated into it. This amelioration mainly benefits from the structure of multistrip FMLF windings that can reduce the consumption of FMLFs. On the whole, compared to the existing approaches, the proposed series of method has a noteworthy superiority in reducing weight and size, Particularly the EMI

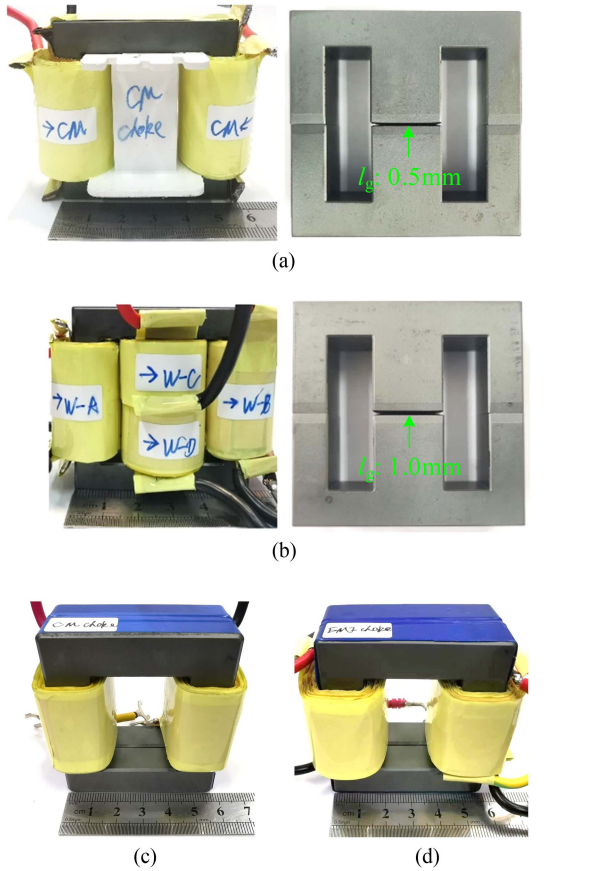

Fig. 27. Prototypes of the (a) proposed CM choke, (b) proposed EMI choke, (c) existing CM choke, and (d) existing EMI choke.

choke, it can reduce weight and volume by 10.3% and 31.2%, respectively, though it has much lower magnetic flux densities.

In addition, a vector network analyzer (VNA) is employed to measure the impedance characteristics of the filter components. In order to reflect the impedance symmetry of the proposed CM and EMI chokes, all their CM or DM components' equivalent impedances and individual impedances relevant to *L*- and *N*-lines are tested.

The impedance characteristics of the CM choke are shown in Fig. 28, in which, the data at 300 kHz are presented for directly reflecting the achieved filtering parameters. As can be seen, the equivalent CM and DM inductances are 2.28 mH, and 493 μH, respectively. Both the practical CM capacitances are around 12 nF, the design deviations are within 1 nF. Furthermore, the impedance curves of individual components demonstrate the structure symmetry and balanced impedances in *L*- and *N*-lines, of the choke. In addition, from Fig. 28(d), the equivalent DM capacitance that formed by CM capacitances is 5.75 nF, which is nearly equal to half of the CM capacitance.

Fig. 29 presents the corresponding impedances of different filtering components in the EMI choke. As expressed in Fig. 29(a), the equivalent CM inductance is about 2.49 mH, which is slightly greater than that of the integrated CM choke. From Fig. 29(b) and (c), it can be seen that the equivalent DM inductance and individual CM capacitance are around 262 μH, and 11.1 nF,

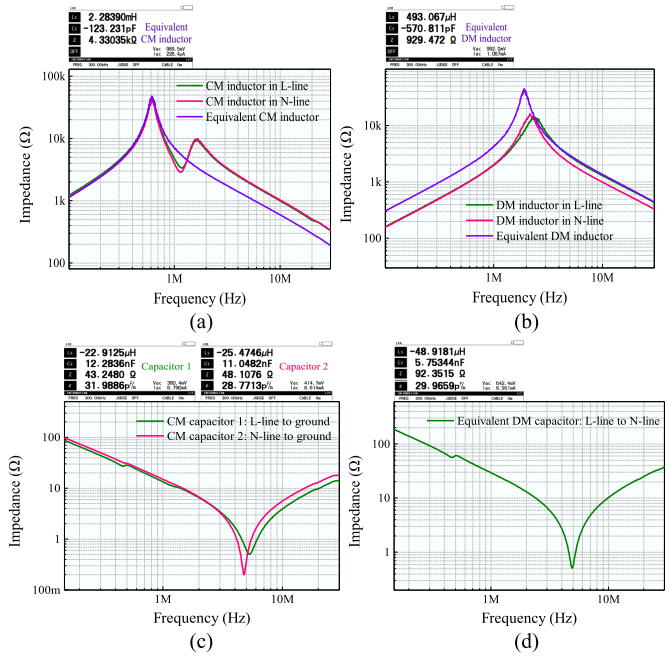

Fig. 28. Impedances of (a) CM inductors, (b) DM inductors, (c) CM capacitors, and (d) equivalent DM capacitor in the proposed CM choke.

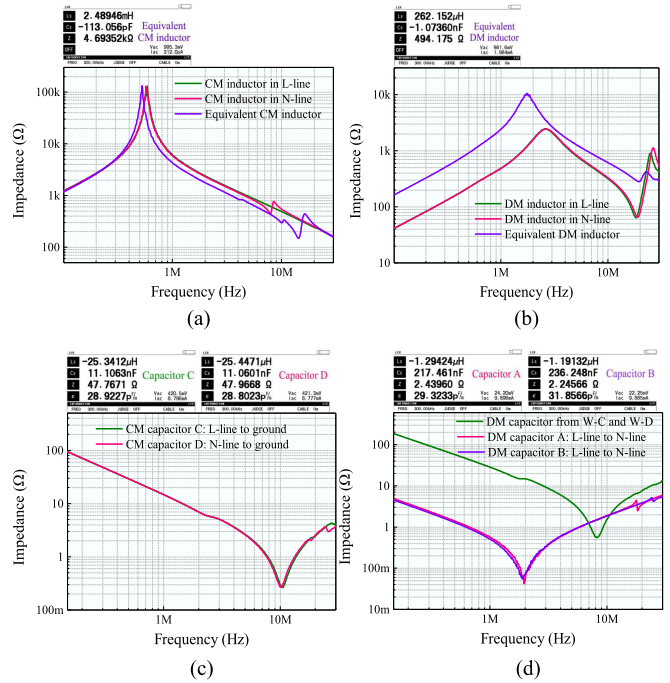

Fig. 29. Impedances of (a) CM inductors, (b) DM inductors, (c) CM capacitors, and (d) DM capacitors in the proposed EMI choke.

respectively. The associated relatively small design errors are generally caused by attribute fluctuations of the used materials and deviations of the fabrication process, which is a common phenomenon in design of passive elements. In addition to the small equivalent DM capacitance provided by CM capacitors, as can be observed from Fig. 29(d), the extra integrated DM capacitances in *W–A* and *W–B* are approximate to 217.5, and

TABLE V
FILTERING PARAMETERS OF THE PROPOSED CM AND EMI CHOKES

Type	Inductor	L	EPC	Capacitor		C	ESL
CM choke	$L_{\text{CM-eq}}$	2.28 mH	31.0 pF	C_{CM}	C_{CM1}	12.3 nF	72.6 nH
	$L_{\text{DM-eq}}$	493.1 μH	14.2 pF		C_{CM2}	11.0 nF	100.8 nH
EMI choke	$L^*_{\text{CM-eq}}$	2.49 mH	42.2 pF	C^*_{CM}	$C_{\text{CM-C}}$	11.1 nF	22.8 nH
					$C_{\text{CM-D}}$	11.1 nF	22.8 nH
	$L^*_{\text{DM-eq}}$	262.2 μH	29.8 pF	C_{DM}	$C_{\text{DM-A}}$	0.22 μF	30.3 nH
					$C_{\text{DM-B}}$	0.24 μF	27.9 nH

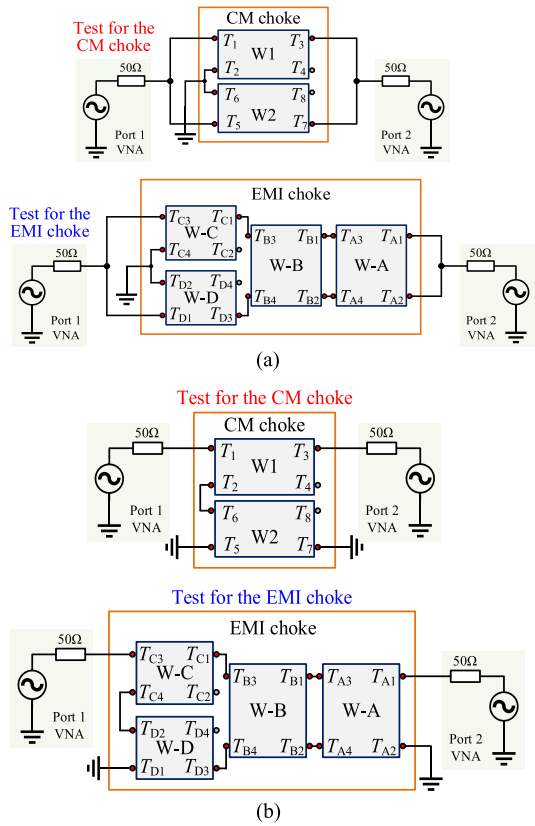

Fig. 30. Experimental configurations to measure (a) CM and (b) DM, ILs of the proposed CM and EMI chokes using a two-port VNA.

236.2 nF, respectively, which have the capability to ameliorate DM noise suppression performance. In addition, as can be seen from Fig. 29(a)–(c), the individual line impedances of the CM inductor are symmetrical, as well as the DM inductors and CM capacitors. Overall, the realized filtering parameters are roughly consistent with the expectations, and the impedances relevant to *L*- and *N*-lines, meanwhile, can reach satisfied balance. From the measurements, filtering parameters of the proposed CM and EMI chokes are given in Table V, which will be used in the following discussions.

Moreover, ILs of the proposed CM and EMI chokes are measured using a two-port VNA, the device configurations for CM and DM measurements are presented in Fig. 30(a) and (b),

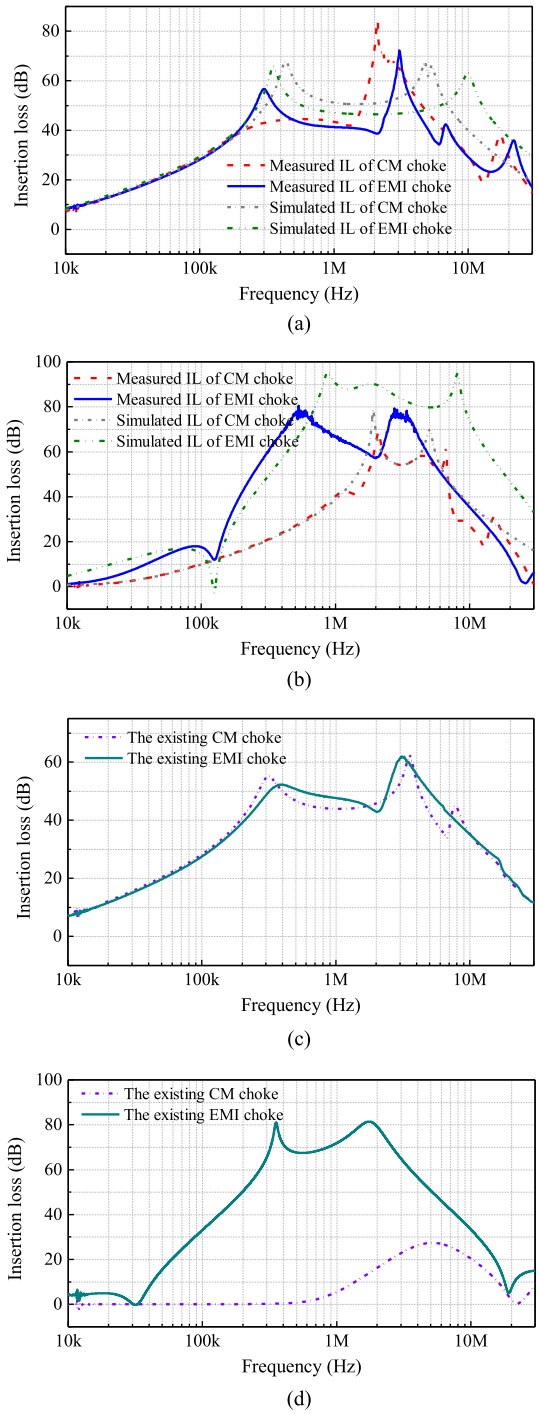

Fig. 31. ILs of the proposed chokes: (a) Common-mode and (b) differential-mode; ILs of the existing chokes: (c) common-mode and (d) differential-mode.

respectively. The extracted CM ILs, as shown in Fig. 31(a), demonstrate the same CM IL objective for both chokes. As it should be, in high-frequency range, there are some inevitable differences that caused by parasitic parameters. By contrast, the differences in DM ILs of the chokes are much more significant. As can be seen from Fig. 31(b), compared to the CM choke, the DM IL of the EMI choke is remarkably raised, especially within the frequency band below 2 MHz. As has been analyzed and indicated in Section III, this modification is mainly contributed by the additionally integrated DM capacitors in *W–A* and *W–B*, which can upgrade the equivalent DM filtering circuit topology from Γ-type (CL) to π-type (CLC). For reflecting the validity of the CM and DM lumped circuits, ILs of the lumped circuits are simulated with LT-Spice software. The simulated CM and DM ILs of the proposed chokes considering the parasitic parameters are presented in Fig. 31(a) and (b), respectively. As can be seen, in relatively low-frequency range, the simulated CM ILs of the CM and EMI chokes are nearly in line with the measured CM ILs, the deviations within 2 MHz are overall less than 10 dB. In terms of DM ILs, the simulated result of the CM choke shows a good consistency with the test result in almost the whole test frequency band; and within 700 kHz, the theoretical IL of the EMI choke is nearly consistent with the test result, but there are great deviations at higher frequencies. There is no doubt that the structures and installations of the filters have some impacts on practical performance of their ILs, especially in high-frequency range. By comparison, the CM choke's lumped filtering circuits have better adaptability, which mainly benefits from its simpler compositional structure. Additionally, Fig. 31(c) and (d) shows the CM and DM ILs, respectively, of the existing CM and EMI chokes. It can be seen that both the chokes have the similar CM ILs as the proposed chokes, which meets the design objective. As can be seen, in this case, the existing CM choke has quite limited DM IL since no additional DM filtering components are integrated in the unit. The existing EMI choke can significantly increase the DM IL, here, it is worth mentioning that the DM IL characteristic has some differences with that of the proposed one owing to the different distributions of the DM capacitors.

C. Practical Performance

Experimental tests of the ac-side conducted EMI emissions of the inverter system under different conditions are carried out, the circuit diagram and system configurations are illustrated in Fig. 32. A (50 μH + 5Ω)‖50Ω single-phase V-network LISN with an embedded CM&DM separator is employed to extract CM, DM, and total conducted emissions. In this article, standard EN55011-class B, which is referenced in the prototype design, is set as the test standard.

Fig. 33 presents the CM conducted EMI of the system with different experimental configurations. As can be seen from Fig. 33(a), the CM noise is quite low (its peak values are much smaller than 40 dBμV in the entire measurement frequency range) when the system is in OFF-state, but it shows a marked deterioration when the system operates at rated power without EMI filter. Fig. 33(b) and (c) presents the corresponding CM EMI spectrums of the system with the proposed CM and EMI chokes, respectively. As can be seen, both chokes have the similar CM noise attenuation performance. Within 10 MHz, the quasi-peak and average CM EMI levels can be reduced to below the relevant limits with any one of them. Only the EMI amplitudes at some frequencies over 10 MHz are not restrained sufficiently.

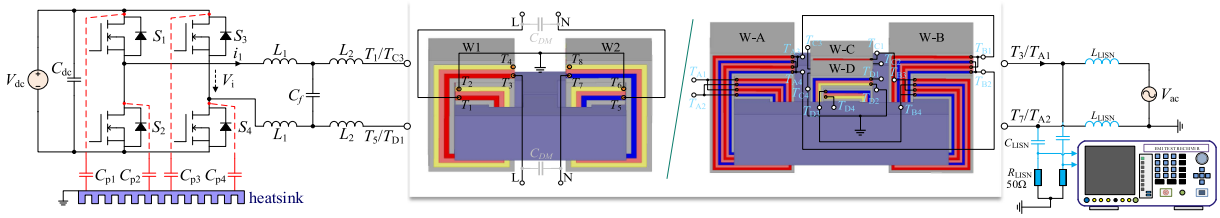

Fig. 32. Configuration of the inverter prototype with the designed EMI filters.

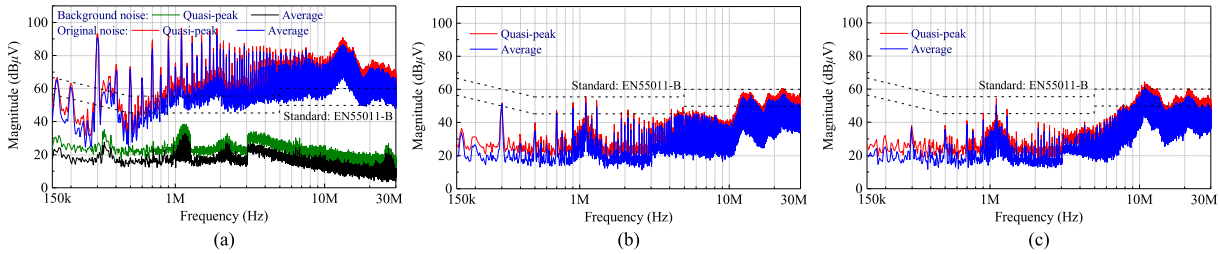

Fig. 33. Experimental measurements of the CM conducted emissions. (a) Without EMI filter, with the proposed (b) CM and (c) EMI chokes.

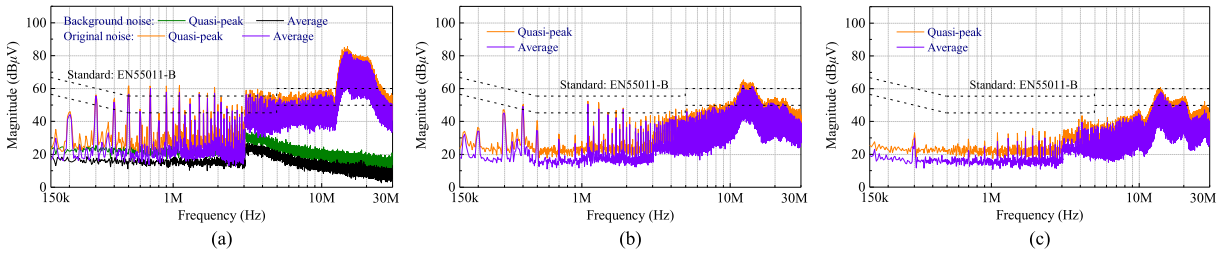

Fig. 34. Experimental measurements of the DM conducted emissions. (a) Without EMI filter, with the proposed (b) CM and (c) EMI chokes.

The measured DM conducted EMI spectrums are shown in Fig. 34. As can be seen from Fig. 34(a), compared to the original CM EMI, the original DM EMI issue is much mitigatory, which mainly benefits from the front-end *LCL* harmonic filter. It can be observed from Fig. 34(b) that the DM noise attenuation at some frequencies (containing both low and high frequencies) is still inadequate though the CM choke has a great DM EMI noise suppression ability. By contrast, DM attenuation capacity of the EMI choke is much better. The comparison between Fig. 33(b) and (c) validates the higher DM noise attenuation of the EMI choke within 5 MHz, which is in line with the performance differences that revealed by the extracted DM ILs.

In theory, the more symmetrical the total EMI noise in *L*- and *N*-lines, the smaller the DM noise, then the more consistent the total EMI noise with the CM EMI noise. As is well known, the balanced impedances in power lines can contribute to reducing DM EMI noise, which is conducive to avoiding excessive total noise in one of the power lines. Spectrums of total conducted EMI noise of the inverter system are shown in Fig. 35, the total EMI emissions in *L*- and *N*-lines are nearly the same since the DM noise is relatively much smaller. Therefore, as can be seen, the total EMI noise is quite similar to the corresponding CM EMI noise, especially when the EMI choke is adopted. On the whole, both chokes can markedly mitigate the total EMI noise. In addition, EMI of the system with the existing CM and EMI chokes are measured. It can be seen from Fig. 36(a) and (b) that both the existing chokes have the similar CM noise suppression capacities as the proposed chokes. However, as shown in Fig. 36(c), DM noise attenuation of the existing CM choke is very inadequate, especially in low frequency band (within 1 MHz). Although the relevant ability of the existing EMI choke shown in Fig. 31(d) looks much better, the positive performance cannot be played so well in practice. As can be seen from Fig. 36(d), there exists noise amplification phenomena at some sensitive frequencies of the CM noise. As has been indicated in Section II, this negative performance is mainly caused by asymmetry of the circuit's filtering inductors in the two power lines, which tends to induce CM-to-DM noise conversion.

Finally, the system efficiencies with different types of EMI filters are extracted. As shown in Fig. 37, under the same output power, the system with the existing CM choke has the highest

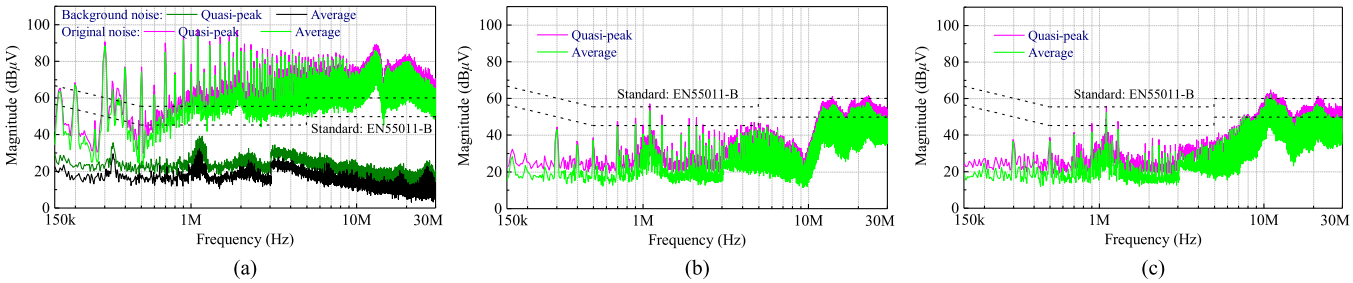

Fig. 35. Experimental measurements of the total conducted emissions. (a) Without EMI filter, with the proposed (b) CM and (c) EMI chokes.

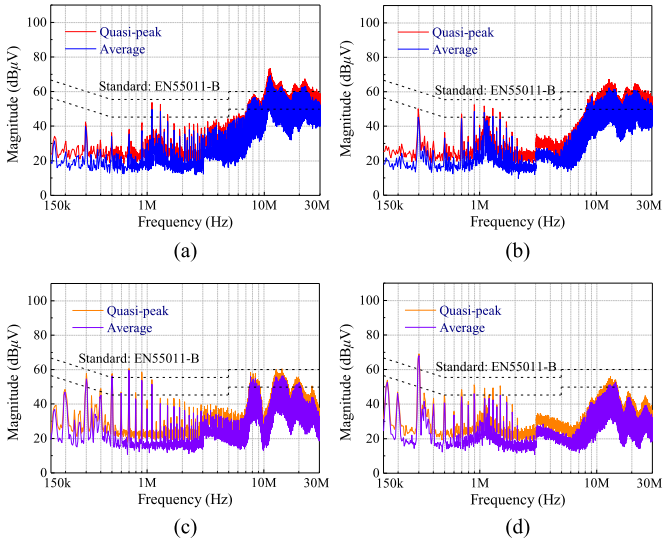

Fig. 36. Experimental measurements of the CM conducted emissions with the existing (a) CM choke, (b) EMI choke; DM conducted emissions with the existing. (a) CM choke. (b) EMI choke.

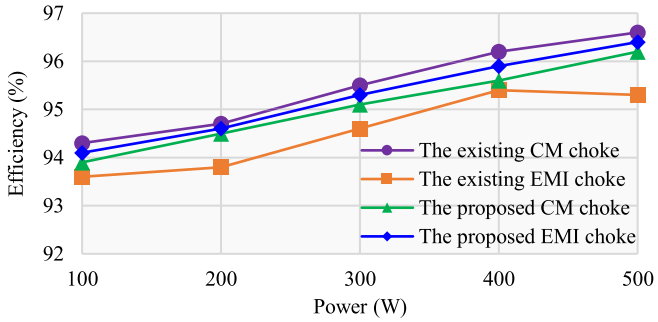

Fig. 37. Efficiency of the inverter system with different EMI filters.

efficiency, this is because no DM inductor is designed. While, compared to the existing EMI choke, the proposed method can improve the system efficiency to some degree, which indicates the superiority of the proposed chokes in decreasing power loss. The proposed CM and EMI chokes can achieve similar system efficiencies, the slight improvement of the EMI choke mainly profits from the less core loss introduced by the lower magnetic flux density.

VI. Conclusion

In this article, the full integration models for a specific CM choke and a complete EMI choke are designed, respectively, using the FMLF techniques and EE-type cores. All the CM inductor, CM capacitors and DM inductors are integrated into the CM choke with two common single-strip FMLF windings. The DM inductances are provided by leakage inductances of the CM inductor, which can be controlled by regulating the air gap length in the EE core's central leg. Compared to the CM choke, the EMI choke further integrates two DM capacitors, which are associated with the CM inductors through two well-designed multistrip FMLF windings. Moreover, the DM inductors are combined with the CM capacitors, which are achieved by two single-strip windings on central-leg of the core, instead of CM inductor's leakage inductances. In addition, both the chokes can attain balanced impedances in power lines, which are conducive to mitigating the EMI issues. Comparative experiments have been carried out to demonstrate the feasibility and validity of the proposed methods. The practical tests of some key indices indicate that the proposed EMI choke has greater superiorities in reducing weight, volume and power losses, while achieving higher DM noise attenuation. But meanwhile, it is much more difficult to design the EMI choke owing to the more complex integrated structure, which generally takes more time for the design. Hence, for practical applications, the used choke type is recommended to be reasonably selected from the proposed CM and EMI choke according to the specific cases.

References

[1] A. K. Morya et al., "Wide bandgap devices in AC electric drives: Opportunities and challenges," *IEEE Trans. Transp. Electrific.*, vol. 5, no. 1, pp. 3–20, Mar. 2019.

[2] B. Zhang and S. Wang, "A survey of EMI research in power electronics systems with wide-bandgap semiconductor devices," *IEEE J. Emerg. Sel. Topics Power Electron.*, vol. 8, no. 1, pp. 626–643, Mar. 2020.

[3] Y. Zhang, Y. Shi, and H. Li, "EMI noise separation method for three-phase WBG inverters with low sensitivity to parasitic parameters," *IEEE Trans. Power Electron.*, vol. 33, no. 6, pp. 4589–4593, Jun. 2018.

[4] *Electromagnetic Compatibility (EMC) - Part 4-6: Testing and Measurement Techniques - Immunity to Conducted Disturbances, Induced by Radio-Frequency Fields*, IEC 61000-4-6:2003 + A1:2004 A2:2006, 2007.

[5] *Industrial, Scientific and Medical Equipment. Radio-Frequency Disturbance Characteristics. Limits and Methods of Measurement*, BS EN 55011 AMD 2, 2018.

[6] R. Lai, Y. Maillet, F. Wang, S. Wang, R. Burgos, and D. Boroyevich, "An integrated EMI choke for differential-mode and common-mode noise suppression," *IEEE Trans. Power Electron.*, vol. 25, no. 3, pp. 539–544, Mar. 2010.

[7] F. Luo, D. Boroyevich, P. Mattevelli, K. Ngo, D. Gilham, and N. Gazel, "An integrated common mode and differential mode choke for EMI suppression using magnetic epoxy mixture," in *Proc. IEEE Appl. Power Electron. Conf. Expo.*, 2011, pp. 1715–1720.
[8] W. Tan, C. Cuellar, X. Margueron, and N. Idir, "A common-mode choke using toroid-EQ mixed structure," *IEEE Trans. Power Electron.*, vol. 28, no. 1, pp. 31–35, Jan. 2013.
[9] Y. Liu, S. Jiang, W. Liang, H. Wang, and J. Peng, "Modeling and design of the magnetic integration of single- and multi-stage EMI filters," *IEEE Trans. Power Electron.*, vol. 35, no. 1, pp. 276–288, Jan. 2020.
[10] J. Borsalani, A. Dastfan, and J. Ghalibafan, "An integrated EMI choke with improved DM inductance," *IEEE Trans. Power Electron.*, vol. 36, no. 2, pp. 1646–1658, Feb. 2021.
[11] Z. Lingyin and J. D. v. Wyk, "Frequency-domain modeling of integrated electromagnetic power passives by a generalized two-conductor transmission structure," *IEEE Trans. Circuits Syst. I Reg. Papers*, vol. 51, no. 11, pp. 2325–2337, Nov. 2004.
[12] Z. Lingyin and J. D. v. Wyk, "The modeling of planar multi-cell integrated reactive components based on multi-conductor generalized transmission structure theory," in *Proc. Conf. Rec. 37th IEEE IAS Annu. Meeting*, 2002, vol. 3, pp. 1787–1794.
[13] C. Rengang, J. D. v. Wyk, S. Wang, and W. G. Odendaal, "Planar electromagnetic integration technologies for integrated EMI filters," in *Proc. IEEE Ind. Appl. Conf.*, 2003, vol. 3, pp. 1582–1588.
[14] C. Rengang, J. D. Van Wyk, W. Shuo, and W. G. Odendaal, "Improving the characteristics of integrated EMI filters by embedded conductive layers," *IEEE Trans. Power Electron.*, vol. 20, no. 3, pp. 611–619, May 2005.
[15] S. Wang and C. Xu, "Design theory and Implementation of a planar EMI filter based on annular integrated inductor–capacitor unit," *IEEE Trans. Power Electron.*, vol. 28, no. 3, pp. 1167–1176, Mar. 2013.
[16] H.-F. Huang, L.-Y. Deng, B.-J. Hu, and G. Wei, "Techniques for improving the high-frequency performance of the planar CM EMI filter," *IEEE Trans. Electromagn. Compat.*, vol. 55, no. 5, pp. 901–908, Oct. 2013.
[17] X. Wu, D. Xu, Z. Wen, Y. Okuma, and K. Mino, "Design, modeling, and improvement of integrated EMI filter with flexible multilayer foils," *IEEE Trans. Power Electron.*, vol. 26, no. 5, pp. 1344–1354, May 2011.
[18] C. Deng et al., "Integration of both EMI filter and boost inductor for 1-kW PFC converter," *IEEE Trans. Power Electron.*, vol. 29, no. 11, pp. 5823–5834, Nov. 2014.
[19] C. Deng, M. Yong, L. A. G. Rodriguez, J. C. Balda, and R. Li, "Passive integration using FMLF technique for integrated boost resonant converters," *IEEE Trans. Ind. Electron.*, vol. 67, no. 5, pp. 3756–3766, May 2020.
[20] J. Ma, W. Zhong, P. Chen, Y. Chen, and D. Xu, "An optimization design of output filter in a grid connected inverter with flexible multilayer foil technique," *IEEE Trans. Energy Convers.*, vol. 34, no. 1, pp. 221–231, Mar. 2019.
[21] S. Jiang, W. Wang, P. Wang, and D. Xu, "A fully integrated common-mode choke design embedded with differential-mode capacitances," *IEEE Trans. Power Electron.*, vol. 37, no. 5, pp. 5501–5513, May 2022.
[22] C. Deng, S. Li, and J. Tang, "A review of flexible multilayer foil integration technology for passive components," *IEEE Trans. Power Electron.*, vol. 36, no. 11, pp. 13025–13038, Nov. 2021.
[23] S. Jiang, Y. Liu, X. Ye, and X. Pan, "Design of a fully integrated EMI filter for a single-phase grid-connected inverter," *IEEE Trans. Ind. Electron.*, vol. 68, no. 12, pp. 12296–12309, Dec. 2021.
[24] S. Jiang, Y. Liu, Z. Mei, J. Peng, and C.-M. Lai, "A magnetic integrated LCL–EMI filter for a single-phase SiC-MOSFET grid-connected inverter," *IEEE J. Emerg. Sel. Topics Power Electron.*, vol. 8, no. 1, pp. 601–617, Mar. 2020.

Shiqi Jiang (Student Member, IEEE) received the B.S. degree in automation science from Hubei University of Technology, Wuhan, China, in 2017, and the M.S. degree in control engineering from Shenzhen University, Shenzhen, China, in 2020. He is currently working toward the Ph.D. degree in electrical engineering with the School of Electrical Engineering and Automation, Harbin Institute of Technology (HIT), Harbin, China.

His current research interests include EMI/EMC, passive integration technique, and sensorless control of grid-connected converters.

Panbao Wang (Senior Member, IEEE) received the M.S. and Ph.D. degrees in electrical engineering from the Harbin Institute of Technology (HIT), Harbin, China, in 2011 and 2016, respectively.

In 2017, he was an Assistant Professor with the Department of Electrical Engineering, HIT. Since 2020, he has been an Associate Professor with the Department of Electrical Engineering, HIT. His research interests include distributed control and optimal operation of microgrids, and highly integrated power electronics converters, etc.

Wei Wang (Member, IEEE) received the B.S. degree in automatic test and control, the M.S. degree in electrical engineering, and the Ph.D. degree in mechanical electronic engineering from the Harbin Institute of Technology (HIT), Harbin, China, in 1984, 1990, and 2002, respectively.

Since 2003, she has been a Professor with the Department of Electrical Engineering, HIT. Her research interests include soft-switching converters, photovoltaic grid-connected inverters, and ac/dc microgrids.

Yitao Liu (Senior Member, IEEE) received the B.S. degree in electrical engineering from Wuhan University, Wuhan, China, in 2008, and the M.S. and Ph.D. degrees in electrical and electronic engineering from Nanyang Technological University, Singapore, in 2009 and 2014, respectively.

From 2014 to 2015, he was a Research Fellow with the Rolls Royce-NTU Joint Laboratory. He is currently an Associate Professor with the College of Mechatronics and Control Engineering, and also with the Guangdong Key Laboratory of Electromagnetic Control and Intelligent Robots, Shenzhen University, Shenzhen, China. His current research interests include high power density converters, EMI/EMC in power electronics, and wideband-gap devices.

Dianguo Xu (Fellow, IEEE) received the B.S. degree in control engineering from Harbin Engineering University, Harbin, China, in 1982, and the M.S. and Ph.D. degrees in electrical engineering from Harbin Institute of Technology (HIT), Harbin, China, in 1984 and 1989, respectively.

In 1984, he was an Assistant Professor with the Department of Electrical Engineering, HIT. Since 1994, he has been a Professor with the Department of Electrical Engineering, HIT. He was the Dean with the School of Electrical Engineering and Automation, HIT, from 2000 to 2010. From 2014 to 2020, he was the Vice President with HIT. He has authored/coauthored more than 1000 technical papers. His research interests include renewable energy generation technology, power quality mitigation, sensor less vector-controlled motor drives, and high-performance PMSM servo system.

Dr. Xu is currently an Associate Editor for IEEE TRANSACTIONS ON POWER ELECTRONICS, THE IEEE TRANSACTIONS ON INDUSTRIAL ELECTRONICS, and the IEEE JOURNAL OF EMERGING AND SELECTED TOPICS IN POWER ELECTRONICS. He is currently the Chairman of IEEE Harbin Section. He is the recipient of the 2018 IEEE Industry Applications Society Outstanding Achievement Award.